Princeton Plasma Physics Laboratory

PPPL- 5112

PPPL-5112

Variations in Edge and SOL Turbulence in NSTX

S.J. Zweben, W.M. Davis, S.M. Kaye, J.R. Myra, R.E. Bell, B.P LeBlanc, R.J. Maqueda, T. Munsat, S.A. Sabbagh, Y. Sechrest, D.P. Stotler, and the NSTX Team

January 2015

PPPL PRINCETON PLASMA PHYSICS LABORATORY

Prepared for the U.S. Department of Energy under Contract DE-AC02-09CH11466.

Princeton Plasma Physics Laboratory
Report Disclaimers

Full Legal Disclaimer

Trademark Disclaimer

PPPL Report Availability

Princeton Plasma Physics Laboratory:

http://www.pppl.gov/techreports.cfm

Office of Scientific and Technical Information (OSTI):

http://www.osti.gov/scitech/

Related Links:

U.S. Department of Energy

Office of Scientific and Technical Information

Variations in Edge and SOL Turbulence in NSTX

S.J. Zweben[1*], W.M. Davis[1], S.M. Kaye[1], J.R. Myra[2], R.E. Bell[1], B.P LeBlanc[1], R.J. Maqueda[1**], T. Munsat[3], S.A. Sabbagh[4], Y. Sechrest[3], D.P. Stotler[1] and the NSTX Team

[1]Princeton Plasma Physics Laboratory, Princeton NJ 08540 USA
[2]Lodestar Research Corporation, Boulder, CO, USA
[3]Department of Physics, Univ. of Colorado, Boulder CO 80309 USA
[4] Dept. of Appl. Phys. and Appl. Math, Columbia Univ., New York, NY10026 USA

footnote: *szweben@pppl.gov
footnote: **presently at X Science LLC, Plainsboro, NJ 08543 USA

Abstract

This paper describes the range of variations in edge and SOL turbulence observed using a gas puff imaging (GPI) diagnostic in NSTX discharges. The database consists of 140 shots including Ohmic, L-mode, and H-mode plasmas measured during steady-state conditions (e.g. without ELMs). Turbulence quantities were evaluated using both cross-correlation analysis and blob tracking. Relative fluctuation levels varied from ~15-100%, correlation times were ~15-40 μsec, correlation lengths were L_{pol}~ L_{rad}~5-10 cm, and turbulence velocities were V_{pol}~2±1 km/sec and V_{rad}~0.5±0.5 km/sec outward. These variations were evaluated as a function of both the global and local edge plasma parameters, and compared with simplified theoretical models.

1. Introduction

Edge and scrape-off-layer (SOL) turbulence is important in tokamaks because it affects the edge plasma profiles and the location of the plasma loss to the wall. The edge plasma profiles in turn affect the core plasma and fusion performance, and the location of heat and particle flux strongly influences the design of the divertor and first wall. Thus it would be useful to understand the existing variations in edge and SOL turbulence well enough to predict the edge transport in future devices.

The goal of this paper is to provide a detailed description of the variations in the edge and SOL turbulence in NSTX, a mid-sized spherical tokamak at PPPL [1]. The present analysis covers a wide database of turbulence measurements made during the steady-state periods of Ohmic, L-mode, and H-mode discharges. The specific motivation for this paper is to determine how the edge turbulence varies with the global and local plasma parameters, how the turbulence characteristics are related to each other, and how well these turbulence variations can be described by simplified theoretical models.

To provide an introduction for the present paper, this section briefly summarizes prior review papers on this topic, and then summarizes the previous work in this area on NSTX. Further relationships between the present results and previous results are discussed in Sec. 6.5

Two early reviews [2,3] noted that the relative fluctuation level for various tokamaks increased with minor radius from $\tilde{n}/n < 1\%$ in the core to $\tilde{n}/n \sim 30\%$ at the edge, roughly consistent with the wave breaking (mixing length) limit $\tilde{n}/n \sim 1/k_{perp}L_n$, where k_{perp} is the radial wavenumber of the turbulence and L_n is the local density scale length. They also noted that the turbulence size scale was in the range $k_{perp}\rho_s < 1$, where ρ_s is the drift-wave gyroradius parameter, and the frequencies were in the range $\omega \sim k_{perp}v_{drift,}$ where v_{drift} is the diamagnetic drift velocity. These results were both roughly consistent with drift-wave turbulence theory, and these same theoretical characterizations of turbulence are still used in the discussion of the present data (Secs. 5.2-5.3).

A subsequent review highlighted edge turbulence results from Ohmic discharges in TEXT [4] The estimated turbulent convection in the SOL as measured by probes accounted for a significant fraction of the electron heat flux in the SOL, and a reversal of the poloidal velocity of the edge turbulence vs. minor radius was found across the separatrix. However, no satisfactory model was found which predicted all the measured features of edge turbulence. A more recent review of edge turbulence in toroidal fusion devices [5] found the poloidal size scale range was $k_{pol}\rho_s \sim 0.02\text{-}0.1$, and noted some exceptions to the wave breaking fluctuation limit, e.g. the high fluctuation level in the flat density region in the far-SOL. No clear plasma current or q(a) scaling was found across machines, consistent with the similarity of edge turbulence in tokamaks, stellarators, and RFPs. Another recent review highlighting DIII-D results [6] reiterated that a definitive scaling of edge turbulence with plasma or machine parameters has not yet been obtained.

Experimental results and theory of the discrete "blob-filament" structures as seen in the edge of tokamaks and other devices were summarized in another recent review [7]. Tokamak blob sizes were ~0.5-4 cm (half-width), and radial blob velocities were ~0.2-3 km/sec, bounded by the inertial and sheath-limited blob models (see Sec. 6.4). More recently, variations of edge turbulence from five stellarators and two tokamaks in L-mode showed systematic variations with the drift-wave parameters for both the edge and SOL, and outward blobs transport in the SOL in all devices [8].

Previous NSTX papers have described the edge turbulence in steady-state conditions as measured by GPI. Initial comparisons were made of Ohmic, L-mode and H-mode plasmas, along with some analysis of blobs [9]. Correlation lengths and turbulence velocities across the L-H transition were described for one plasma condition [10]. The intermittency in the SOL during H-modes was studied at power levels from P_{NBI} = 0-6 MW [11], with the lowest blob activity in Ohmic H-modes. A scan of lithium coating resulted in a relatively small increase in edge turbulence velocity [12]. Most recently, the effect of the GPI gas puff itself was studied and little or no effect was seen on the edge plasma or edge turbulence at the peak of the GPI puff [13].

Several theoretical analyses of the GPI results on NSTX have been published by Lodestar group. The first paper [14] focused on a small set of blobs in L-mode and H-mode shots, and compared their radial motion with analytic blob models for convection. Subsequently, a reduced 2D edge turbulence simulation model was made using the SOLT code [15] and initial results were compared with fluctuation levels, blob structure, and heat flux SOL width measurements. A synthetic GPI diagnostic was added to SOLT [16] and further comparisons with GPI were made, including a sensitivity study with respect to various theoretical assumptions. Finally, SOLT simulations and GPI data were compared with respect to the effect of edge sheared flows on blobs [17], and detailed GPI blob tracking for one NSTX shot was interpreted in terms of edge shear flows.

The present paper describes the variations of edge turbulence in NSTX over a much larger database than previous papers. The outline is as follows: Section 2 describes the database and data analysis methods, Sec. 3 describes the results from turbulence cross-correlation analysis, Sec. 4 describes the results from blob analysis, and Sec. 5 contains discussion of these results and their transport implications. Section 6 describes comparisons with theory and with previous experimental results, and Sec. 7 contains the conclusions and suggested directions for further research.

2. Database and data analysis

2.1 Database selection

The database used in this paper contains 140 NSTX discharges from the 2010 run, each of which had a single deuterium GPI gas puff during the constant-current period of the shot. The range of global plasma parameters is given in Table I. All discharges were made in deuterium with a major radius R~85 cm, minor radius a~65 cm, carbon plasma-

facing surfaces with lithium conditioning, with a toroidal magnetic field on axis from B_t=3.5-5.5 kG and a plasma current of I_p=0.65-1.15 kA. This database includes shots from about 17 separate experiments covering most of the range of NSTX operation. Of these 140 shots, 93 were in H-mode (all with NBI), 33 were Ohmic, and 14 in L-mode (9 with NBI only and 5 with RF). All shots had an elongated magnetic equilibrium with κ~1.9-2.5 and q_{95}=5.8-12.8. Nearly all shots (93%) had a lower single-null divertor shape (the rest having double-null or upper-single-null).

The turbulence was analyzed during a 10 msec period at the peak of the GPI gas puff in these discharges. The shots used in the database were selected by the following criteria, which were applied from 10 msec before to 5 msec after the peak of the GPI signal: constant plasma current, magnetic field, and applied heating power; absence of large MHD activity such as ELMs or large coherent MHD modes; absence of L-H or H-L transitions; good GPI signal levels (GPI gas puff ~3-6 Torr-liters); appropriate B field-line angle for GPI viewing along B (i.e. I_p/B_t = 0.2±0.05 MA/kG); constant outer separatrix position (to within ±1 cm), with at least 3 cm inside the separatrix visible within the GPI field of view; and GPI data taken at the fastest available camera rate (397,660 frames/sec). About half of the shots taken at this GPI framing rate satisfied the other conditions. This database included some shots which were previously used for GPI analysis of the turbulence velocity vs. lithium [12], comparisons of GPI with DEGAS 2 [18], comparisons of GPI with SOLT [17], and the gas puff effects of GPI [13].

A table of the parameters in this database can be found at [NF supplementary material]. A web site [PPPL web site] shows the time dependences of various plasma parameters, the GPI signal levels, and sample GPI movies for each shot.

2.2 Gas puff imaging diagnostic

The present NSTX GPI diagnostic is the same as described previously [13]. A fast Phantom 710 camera viewed a 30 cm poloidal by 24 cm radial region in the plane perpendicular to the local B field just above the outer midplane near the separatrix. A gas manifold attached to the nearby wall puffs deuterium gas into this region, and the Dα light from the neutral deuterium from this puff is viewed through a 657 nm (9 nm FWHM) optical filter at 397,660 frames/sec using an 80x64 pixel array. The integration time for each frame is 2.1 μsec, the time between frames was 2.5 μsec, and the spatial resolution of the optical system was ~0.5 cm at the GPI gas cloud.

Sample images of the normalized GPI Dα light emission vs. time are shown in Fig. 1 for a typical H-mode shot with 4 MW of NBI (#140395). The time between these images is ~10 μsec (4 frames), they are oriented so that the poloidal direction is vertical (ion diamagnetic direction down), and the radial direction is horizontal (outward to the right). The relative amplitude of the local fluctuations is normalized to the time-averaged of all image averaged over 1 msec, with the normalized amplitude shown by the color scale. The location of discrete blobs in each frame (defined in Sec. 2.4) is shown by the

black ellipses. The magnetic separatrix is the dashed line and the shadow of the limiter (RF antenna) is the black line in each frame.

Although the GPI data is digitized for ~80 msec per shot, the data analyzed in this paper focuses on time periods within 10 msec of the peak GPI gas puff rate, which includes 4000 frames (i.e. 40 MB of data per shot). This is the time of the maximum GPI signal level (typically 20 times the pre-puff Dα level), and also a time when the perturbation of the gas puff on the edge plasma was found to be negligible [13]. Typical signals levels are within 500-1500 counts per pixel in the region of maximum brightness in these 12 bit camera images.

2.3 Sample edge profiles

Sample profiles of edge electron temperature and density derived from Thomson scattering data are shown in Fig. 2(a) and 2(b). These plots show the results from 7 similar Ohmic shots (with no NBI) and 7 similar H-mode shots (with 4 MW of NBI). This data was taken near the time of peak GPI signal, and is plotted with respect to the outer midplane separatrix determined from the EFIT equilibrium reconstruction code. The shot-to-shot variations in the midplane separatrix position were within 0.5 cm for both H-mode and Ohmic groups. The maximum variation of the separatrix position for reconstructions of nearby equilibria were 0.73 cm for the H-mode cases and 0.21 cm for the Ohmic cases. In these cases and in general, the accuracy of the EFIT separatrix position is estimated to be about ±1 cm.

Overlaid in both Fig. 2(a) and 2(b) are the radial profiles of the GPI Dα light emission signals (in arbitrary units) for typical shots in these series (#140389 and 141746). The GPI signal levels peaked within about ±2 cm of the separatrix in these cases, and the normally extend at least ±4 cm around the separatrix. The GPI data in this paper was analyzed over the radial range from 2 cm inside to 4 cm outside the separatrix. Note that similar GPI Dα profiles and their absolute magnitude were previously well fit by DEGAS 2 modeling based on the Thomson data in H-mode plasmas [18].

A summary of the plasma and edge parameters for these shots is in Table 2, along with the estimated ρ_s, τ_{ei}, and β_e at 2 cm inside the separatrix (i.e. ρ=-2 cm), using the magnetic field on axis to evaluate ρ_s and β_e. The average electron temperatures 2 cm inside the separatrix were T_e~134 eV for H-mode and T_e~23 eV for Ohmic plasmas, and near the separatrix they were T_e ~29 eV for H-mode and T_e~13 eV for Ohmic. Thus there was a significant variation in temperature (and density) between these sample plasmas, which were somewhat less than the range of edge parameter variations in this database.

2.4 Turbulence analysis methods

Edge turbulence cross-correlation and blob-tracking analysis was done for each of the 140 shots in the GPI database of Table 1. These analyses were averaged over ±5

msec around the peak GPI signal, during which time the turbulence quantities were nearly constant. The methods used in these analyses are described in this section, the results are described in Sections 3 and 4, and compared with each other in Sec. 4.4.

The cross-correlation analysis methods used time series of the GPI signal from small regions of the image to calculate the local fluctuation levels, correlation lengths, and turbulence velocities. These analyses average over the entire spectrum of turbulence size scales and timescales, i.e. this method does not track individual 'blob' structures. These time series were derived from averaging over 4x4 pixels (1.5 cm x 1.5 cm) near the vertical middle of the GPI images, i.e. over regions much smaller than the correlation lengths of the turbulence. This local correlation analysis was centered at four different radii with respect to the separatrix, namely at ρ = -2 cm, 0 cm +2 cm and +4 cm. The point at ρ = -4 cm was not used since it was sometimes far inside the peak of the GPI signal level, as for the H-mode cases in Fig. 2.

Sample frequency spectra of these GPI signals at ρ = -2 cm and +2 cm are shown in Fig. 2(c) and 2(d), averaged over the Ohmic and H-mode shots used for the profiles in Figs. 2(a) and 2(b). As usual, these frequency spectra are broadband over the range ~1-100 kHz, indicating the dominance of turbulence in these signals. The details of the spectral shapes are interesting, but only the autocorrelation times will be discussed in this paper. The autocorrelation times for these spectra are in the range ~10-40 μsec, corresponding roughly to the inverse of the mean frequencies.

The relative GPI fluctuation levels $\delta I/I$ (rms/mean) were calculated from standard statistics, and the autocorrelation times (FWHM) were calculated from time-delayed cross-correlation functions. The correlation lengths L_{pol} and L_{rad} (FWHM) were calculated using the zero-time-delay cross-correlation coefficient C_{12} between two 4x4 pixel time series separated by δx_{12}=2.4 cm in either the poloidal or radial direction from the center of the locations used to calculate $\delta I/I$. The correlation lengths were estimated assuming a Gaussian spatial cross-correlation function to be $L_{12}=1.66\ \delta x_{12}/(-\ln C_{12})^{1/2}$. Theses correlation lengths were nearly constant over the analysis time, and averaged over this time for the database. Note that the radial correlation lengths are local estimates at each of the chosen radii, and when these radial correlation lengths are large compared with the radial variations in plasma parameters (as they generally are), this does not imply that the turbulence structure is constant over the radial correlation length.

The turbulence velocities were estimated from the time-delayed cross-correlation functions between time series from individual pixels separated radially or poloidally. Starting from a single pixel at a given radius at the vertical middle of the GPI image, a search was made within the 2D region ±20 pixels poloidally and ±10 pixels radially for the pixel which had the highest cross-correlation coefficient with the starting pixel, given a 1 frame time delay between the two time series. The same process was repeated for 2,3, and 4 frame time delays, i.e. up to a 10 μsec time delay, at which time the maximum cross-correlation coefficients were typically 0.8±0.1. The poloidal and radial locations of these correlation peaks vs. their time delay were fit by a straight line to derive the poloidal and radial turbulence velocities.

The blob tracking analysis was done using a completely different method [17,19]. Figure 1 showed examples of the blob tracking done for this data. All frames are first normalized by the time-average frame in order to identify blobs, i.e. the spatially local maxima in each frame. For the present analysis, a blob is identified when the maximum of the normalized signal is larger than an assumed value of 1.5. The region around each of these maxima is then fit by contours, and an ellipse is fit to the half-maximum contour level. The motion of the central maximum and the shape and tilt of the elliptical fits are then tracked from frame-to-frame. The maximum allowed displacement of a given blob between frames limited to 10 pixels (3.8 cm) to help distinguish different blobs. These blob structures and motions are saved in the database only if they meet these criteria and can be continuously tracked for a lifetime of more than 15 μs. Note that by this (arbitrary) definition a blob can be either inside or outside the separatrix, but this method does not search for negative perturbations ("holes").

Blobs are tracked this way over the entire image, and the results were binned within 2 cm wide regions centered at ρ = -2 cm, 0 cm +2 cm and +4 cm. The blob quantities calculated for each shot were the average number of blobs per frame N_{blob}, the normalized blob amplitudes A_{blob}, the poloidal and radial sizes scales of the blobs L_{pol} and L_{rad}, and the poloidal and radial blob velocities V_{pol} and V_{rad}. These database quantities were averaged over typically several hundred blobs detected within the 10 msec period of interest for each shot.

2.5 Interpretation of GPI turbulence analysis

As discussed previously [20], the measured GPI signal is due to the excitation of the deuterium Dα line, and depends on at least three factors: the local deuterium neutral density, the local electron density, and the local electron temperature. The time-averaged 2-D spatial distribution of the GPI Dα light emission has been calculated using the 3-D Monte Carlo simulation DEGAS, and the resulting 2-D distribution and magnitude of Dα agree well with the time-averaged Dα light in quiescent H-mode discharges [18].

However, the measured GPI fluctuations can not be directly interpreted in terms of the local electron density or temperature fluctuations without some additional assumptions. Thus the turbulence analyses in Sections 3 and 4 use only the GPI Dα signal itself, and do not try to interpret those results in terms of the plasma density or temperature fluctuations. The best way to interpret the measured Dα results with respect to theory or simulation is to convert the predicted turbulence parameters into expected GPI signals using the well-known dependences of Dα on the neutral density and electron density and temperature. This has been done previously when such theoretical turbulence predictions were available [17,21,22], but they were not available for this database.

Nevertheless, some approximate interpretations of the GPI signals can be made. We can assume that where and when the GPI signal level was increased by over a factor-of-10 due to the GPI gas puff (as it was for all the data in this paper), the local neutral density is dominated by the GPI gas puff. Since the neutral gas influx rate from the GPI

puff is constant over turbulence times scales, we will assume that the fluctuations in the GPI signal are dominated by the local electron density and temperature fluctuations. This neglects possible 'shadowing' or modulation of the local neutral density by the local electron density and temperature fluctuations [20], which would tend to be most important radially inside the peak of the Dα emission.

Thus we will assume that the observed fluctuations in the GPI Dα signal are dominated by the local electron density and temperature fluctuations. If these n_e and T_e fluctuations are highly correlated with each other, as predicted from edge turbulence theory [17,21,22], then the local Dα fluctuations should have a simple relationship to the local electron density fluctuations. For example, if the Dα light emission intensity is parameterized as $I=n_o n_e^{\alpha} T_e^{\beta}$, where n_o is the neutral deuterium density, then for small fluctuations $\delta I/I = \alpha(\delta n_e/n_e) + \beta(\delta T_e/T_e)$. If δn_e and δT_e are in phase, then the relative intensity fluctuations $\delta I/I$ are linearly proportional to $\delta n_e/n_e$, with a proportionality constant which depends on α, β, and $\delta n_e/\delta T_e$. If δn_e and δT_e are not in phase, then the resulting δI is a mixture of these two fluctuations and more difficult to interpret.

If $I \sim n_e^{\alpha}$, then there is a direct relationship between the correlation properties of I and n_e. For example, it was shown numerically that the cross-correlation length of a random variable to some power $-2 < \alpha < 4$ is very nearly the same as the cross-correlation of that variable itself [9]. In this case the correlation times, lengths and velocities calculated using cross-correlation functions of GPI light intensity should be the same as those of the density fluctuations, independent of α. This is intuitively clear from our experience with the nonlinear contrast knob on TV monitors; the basic structure and motion of objects does not change when the contrast exponent ("gamma") is changed.

Table 3 shows the exponents α and β for the average electron temperatures and densities at ρ = -2 cm for various types of shots in this database. The density exponent ranges over $\alpha \sim 0.65-0.8$ and the temperature exponent over $\beta \sim 0.1$-0.6 at this radius. In general, over $T_e \sim 5$-200 eV, $\alpha \sim 0.9$-1.0 for $n_e < 10^{12}$ cm^{-3} and $\alpha \sim 0.6$-0.9 for $n_e \sim 10^{12}$ cm^{-3} - 2×10^{13} cm^{-3}. Also, β is nearly independent of density over $n_e \sim 10^{12}$ cm^{-3} - 10^{13} cm^{-3}, but monotonically increases with temperature from $\beta \sim 0.0$-0.1 at $T_e \sim 100$ eV to $\beta \sim 1$ at $T_e \sim$ 10 eV. It should be kept in mind that the practical usefulness of these α and β for interpreting the GPI results is limited due to the large fluctuation levels in edge n_e and T_e, especially in the SOL, and due to the unknown ratio of $\delta n_e/n_e$ to $\delta T_e/T_e$. Some attempt to interpret the δI/I of Secs. 3 and 4 in terms of δn/n is discussed in Sec. 5.1.

3. Turbulence cross-correlation results

This section describes the GPI cross-correlation analysis for this database. Section 3.1 shows the radial profiles, Section 3.2 describes the variations with global parameters, Section 3.3 shows some relationships between turbulence quantities, Sec. 3.4 describes the variations with local edge parameters, and Sec. 3.5 describes a multiple

linear regression analysis using all parameters. Where possible, the results were also sorted according to whether the shots were H-mode, Ohmic, or L-mode (see Table 3).

3.1 Radial profiles

The radial profiles of various statistical quantities derived from the turbulence correlation analysis are shown in Fig. 3, with the error bars giving the shot-to-shot standard deviations over the database for each shot type. The radial profiles of the relative GPI Dα fluctuation levels as shown in Fig. 3(a) increase from $\delta I/I \sim 0.15$-0.3 at 2 cm inside the separatrix to $\delta I/I \sim 0.6$-1.0 at 4 cm outside the separatrix, with about a factor-of-two lower fluctuation levels in H-mode compared to Ohmic or L-mode. The autocorrelation times as shown in Fig. 3(b) increase with radius from $\tau_{auto} \sim 20$ μsec at 2 cm inside the separatrix to $\tau_{auto} \sim 35$ μsec at 4 cm outside the separatrix, with slightly higher autocorrelation times in H-mode compared to Ohmic or L-mode. The poloidal and radial correlation lengths as shown in the Figs. 3(c) and (d) were $L_{pol} \sim L_{rad} \sim 6$ cm in both Ohmic and L-mode, increasing to $L_{pol} \sim 9$ cm in H-mode, and to $L_{rad} \sim 10$ cm in H-mode at 2 cm inside the separatrix.

Typical turbulence poloidal velocities as shown in Fig. 3(e) were $V_{pol} \sim -2 \pm 1$ km/sec in the ion diamagnetic and grad-B drift poloidal drift direction (i.e. downward at the machine), except for a clear reversal to the electron diamagnetic velocity in Ohmic plasma at 2 cm inside the separatrix to $V_{pol} \sim +3.5 \pm 2$ km/sec. In the SOL, these poloidal velocities tend to get closer to zero at larger radii. This velocity as measured in the lab frame may depend on the plasma rotation and the local diamagnetic drift; the variations of V_{pol} with NBI and local pressure gradient are discussed in Secs. 3.2 and 3.4, and a comparison with the diamagnetic velocities is discussed in Sec. 6.3. Radial velocities as shown in Fig. 3(f) were typically $V_{rad} \sim 0.5 \pm 0.5$ km/sec in the outward direction in Ohmic and L-mode, but significantly smaller in H-mode near or outside the separatrix. Variation of V_{rad} with global and local parameters are discussed in Secs. 3.2 and 3.4, and a comparison with theoretical speeds is discussed in Sec. 6.4.

3.2 Variations with global parameters

This section describes how the measured turbulence varies with the global discharge parameters. The approach here is to plot the results from all shots with respect to selected parameters such as line-averaged density to look for rough experimental trends, and then to further separate the data into Ohmic, L-mode and H-mode plasmas where possible. However, since there are 6 turbulence quantities and at least 8 global parameters (see Table 1), only a small fraction the possible cross-plots can be shown explicitly. There are also strong co-variances among some global parameters, such as between the line-averaged density and NBI power, so even if a clear variation is observed, the causal connection between the global variable and the turbulence quantity is not necessarily clear. Note also that the database comes from a broad range of

experiments and not from controlled scans of these global variables, so many parameters may be changing within a single plot.

Some of the basic global parameter variations are shown in Fig. 4. For clarity, here and elsewhere only the data at ρ= -2 cm inside the separatrix and ρ= +2 cm outside the separatrix are plotted. For example, Fig. 4(a) shows that the relative fluctuation level generally decreases with the line-averaged plasma density as $n^{-0.5}$ for both radii, and is significantly smaller inside the separatrix than outside. However, similar trends are seen with neutral beam power and stored energy, which are co-variant (i.e. correlated) with density in this database, due in part to variation from Ohmic plasmas at low density to H-mode plasmas at high density. Figure 4(b) shows that the fluctuation levels also decreases slightly with the amount of lithium applied before the shot, in part because more lithium was used in H-mode plasmas. Figure 4(c) shows that the poloidal velocity V_{pol} inside the separatrix changes direction at the Ohmic-to-H mode boundary at about W=100 kW, and Fig. 4(d) shows that this V_{pol} reversal occurred at ~2 MW of NBI power. Figure 4(e) shows only small variations in the L_{rad} with plasma current, and Fig. 4(f) shows an increase in L_{rad} inside the separatrix at the Ohmic-to-H mode boundary in stored energy.

Table 4 shows linear (pair-wise) cross-correlation coefficients between the six turbulence quantities and 7 global parameters for $\rho = \pm 2$ cm, with correlations above 0.5 highlighted in red and italics. Fairly strong correlations occur between several turbulence quantities and P_{nb}, W, and n_e, but these are also correlated with each other, e.g. n_e and W have a 79% correlation and P_{nb} and W have a 92% cross-correlation, mainly associated with the variation from Ohmic to H-mode. There is a modest correlation between the applied lithium and turbulence, but there are also correlations between lithium and stored energy (54%) and lithium and density (45%), so the causal connection between the lithium level and the turbulence is not clear. There were moderate-to-low correlations between the turbulence and the plasma current and/or toroidal magnetic field, and a significant correlation between L_{pol} and the plasma elongation κ.

Table 5 shows the power-law exponents obtained from single-parameter fits of the turbulence quantities with the global parameters in Table 4, with entries only for cases with a linear cross-correlation >0.5. The relative fluctuation levels decreased with the line-averaged density as $n_e^{-0.5\text{-}0.6}$, as in Fig. 4(a), and the correlation time and lengths inside the separatrix increase as $n_e^{0.55\text{-}0.65}$, with similar but slightly weaker trends vs. stored energy. The dependences on the lithium per shot was quite weak, but there was a surprisingly strong dependence of L_{pol} with κ (although the range of κ was only ~1.9-2.5). The V_{pol} dependence at ρ = -2 cm could not be fit with a power law due to the change in direction with P_{nb}, as shown in Fig. 4(d), and for H-modes shots alone the linear cross-correlation of V_{pol} and P_{nb} was not above 0.5.

3.3 Relationships between turbulence quantities

There are also many possible relationships among the six turbulence quantities, some of which are illustrated in Fig. 5. As in Fig. 4, these plots show all shots in the

database, but for clarity only data points at ρ= -2 cm and ρ= +2 cm are plotted. However, it was not possible to cleanly separate Ohmic, L-mode, and H-mode plasmas for Fig. 5.

Figure 5(a) shows that the radial and poloidal correlation lengths are almost always within a factor-of-two of each other (i.e. between the two lines), but with a slight poloidal elongation for points outside the separatrix. Figure 5(b) shows that the radial velocity is roughly independent of the poloidal velocity for both radii, and Figures 5(c) and 5(d) show that the radial velocity is also roughly independent of the radial correlation length and relative fluctuation level for both radii. Figure 5(e) shows that the poloidal correlation length increases almost linearly with the autocorrelation time for both radii, which suggests they are related by the poloidal velocity. Figure 5(f) shows the measured autocorrelation time τ_{auto} vs. $\tau_{pol}=L_{pol}/V_{pol}$, which is the characteristic time for turbulence to move past a fixed point when $V_{pol}>>V_{rad}$, and where the positive values in Fig. 5(f) come from the positive V_{pol} in Fig. 4(b). About half of the data points are near $\tau_{pol} \sim \tau_{auto}$ (lines shown) indicating "frozen flow" in the poloidal direction, but about half have $\tau_{pol} > \tau_{auto}$, indicating that the turbulence changes before being convected by the poloidal flow over a poloidal correlation length.

3.4 Variations with edge parameters

Local edge parameters were obtained using the Thomson scattering and edge rotation diagnostic (ERD) near the time of these turbulence measurements. Thomson scattering measured the outer midplane electron density and temperature with ~2 cm spatial resolution, and the resulting profiles were smoothed to derive the local edge n_e and T_e and their gradients at 2 cm inside the separatrix for each shot (points at or outside the separatrix had a large uncertainty). The ERD measured the velocity and ion temperature of passively-viewed carbon ions near the peak of the CIII triplet (~465 nm), using separate views in the toroidal and poloidal directions. The CIII line peak was located at an average distance of 2.4±1.9 cm inside the separatrix for the shots in this database (charge exchange ion measurements were not available for this database).

Some of this edge data and its relationship to the edge turbulence are plotted in Fig. 6. Figure 6(a) and 6(b) show that the T_e and n_e at ρ= -2 cm were linearly related, and both increased with NBI beam power. Figure 6(c) shows the relative GPI fluctuation levels decreased with increased local T_e, mainly due to the Ohmic to H-mode variation. Figure 6(d) shows that the relative fluctuation levels also tended to decrease with increasing local gradient $\nabla P_e = n_e \nabla T_e + T_e \nabla n_e$, similar to the dependence on T_e. Figure 6(e) shows that the poloidal velocity at ρ= -2 cm did not vary significantly with the local T_e, except for the positive V_{pol} inside the separatrix seen in Figs. 4(c) and (d). Figure 6(f) shows that the poloidal velocity at ρ= -2 cm has a similar dependence on ∇P_e as it does on T_e alone. There was little or no dependence of the poloidal velocity at ρ= +2 cm on either the T_e or ∇P_e at at ρ= -2 cm.

Data from the ERD is shown in Fig. 7 for 130/140 shots for which the ERD signal peaked between 0 and -5 cm inside the separatrix. Figure 7(a) shows the toroidal and

poloidal carbon edge velocities evaluated at this peak location vs. the NBI injected power. Surprisingly, the average CIII toroidal velocity is -11.5 km/sec in the direction opposite to the NBI direction, while its average poloidal velocity is +0.5 km/sec in the downward (ion diamagnetic drift) direction. Apparently the edge CIII edge rotation is not strongly coupled to the core rotation, which is always in the direction of the NBI. The relationship between the turbulence velocity at ρ= -2 cm and these CIII velocities is shown in Fig. 7(b). There is modest 0.42 linear correlation between the poloidal turbulence velocity at this radius and the toroidal CIII, and a small 0.28 correlation between the poloidal turbulence velocity at ρ= -2 cm and the poloidal CIII velocity.

The cross-correlation coefficients and power law exponents between the turbulence quantities and the edge n_e were shown in Tables 4 and 5 (similar results were obtained for edge T_e since the edge n_e and T_e had a 0.88 correlation). The highest cross-correlations with edge n_e were found for the relative fluctuation levels, which decreased as $\delta I/I \sim n_e^{-0.3}$, and the turbulence correlation lengths at ρ= -2 cm increased as $\sim n_e^{0.3}$. These exponents are similar to but lower than those for the line-averaged densities. The cross-correlations of the turbulence quantities with the CIII edge rotation velocities were generally <0.5, as shown for the toroidal rotation in Table 4, except for a surprising correlation of L_{pol} at ρ= -2 cm with the poloidal CIII velocity (71% correlation).

3.5 Multiple linear regression analysis

Standard multiple linear regression analysis (MLR) was applied to the entire database to fit the turbulence and blob quantities with simultaneous products of power laws of the global and local plasma parameters. In principle, this process could find improved fits with respect to the single-parameter correlations shown in Tables 4 and 5. The turbulence variables used for the fitting were $\delta I/I$, τ_{auto}, L_{pol}, and L_{rad} from the cross-correlation analysis, and the blob number N_{blob}, the blob amplitude A_{blob}, and the blob L_{pol} and L_{rad} from the blob analysis (see Sec. 4). The plasma variables were chosen to be I_p, B_t, line-averaged n_e, lithium/shot, stored energy, kappa, edge n_e, edge dn_e/dR, q_{sep}, and the edge V_{tor} from the CIII measurements. Some variables were not used in these power-law fits since they had negative (i.e. bipolar) values, such as V_{pol}, V_{rad}, and V_{pol} from CIII.

Table 6 shows the statistically significant dependences found from this MLR analysis for the turbulence correlations (top 4 rows) and blob analysis (bottom four rows) at ρ= ±2 cm. The numbers in red and italics had the highest statistical significance, those in black had lower significance, and entries with dashes were not statistically significant. In each box are the power law exponents; for example, the most significant dependences for the relative fluctuation level at ρ=-2 cm are $\delta I/I \sim (B_t)^{-0.88} (dn_e/dR)^{-0.15}$.

Many of the most significant dependences (red entries) in Table 6 were those associated with the plasma elongation κ, as also seen in for single-variable correlations in Table 5; for example, the poloidal correlation length varied as $L_{pol} \sim \kappa^{1.5}$. However, since the range of κ was only κ~1.9-2.5, an exponent of 1.5 implies a variation of only x1.5

over the database. Another significant dependence was $\tau_{auto} \sim n_e^{0.4}$, similar to the result of Table 5 for ρ=-2 cm, and there was a strong negative exponent for the B_t dependence of $\delta I/I$ at ρ=-2 cm, as in Table 5. There were also several statistically significant dependences on the lithium/shot, but the exponents were typically only ~0.1, so changes of x2 in lithium/shot imply a variation of only ~20% in the turbulence quantities. The strong dependences of τ_{auto} and L_{pol} on I_p were surprising, since there were no significant single-parameter correlation of I_p with the these turbulence quantities in Table 4.

The most interesting result from this regression analysis was the consistent dependence of L_{pol} on κ, which seems to suggest a strong flux-surface shaping effect on the edge turbulence structure. The other dependences found in this regression analysis did not provide any clear way to explain the main variations of the turbulence. Note that this MLR analysis does not disentangle the co-variances of W, line-averaged n_e, edge n_e (and other plasma parameters) when they are partially correlated with each other, for example, from Ohmic to H-mode plasmas, so the causal variables in these dependences can not be easily isolated.

4. Blob analysis results

The analysis methods for discrete "blobs" in the edge turbulence are significantly different from the analysis using cross-correlation functions (see Sec. 2.4). Blob analysis is designed to look for structures which are above a threshold in the normalized signal level, arbitrarily chosen to be 1.5 for this paper, and to track these large structures as they move across the GPI image. The physics of discrete blobs in the SOL of a tokamak can also be different from that of the broadband turbulence [7]. Note that the blob tracking algorithm used in this paper does not distinguish between blobs inside or outside the separatrix, and it tracks only positive blobs (and not negative "holes").

Figure 8 shows two examples of blob tracking, one for an Ohmic shot in (a) and the other for an H-mode shot in (b). Each colored line represents one blob track, and the small ellipses show the blob shape and location when it was first identified. Most blobs start inside or near the separatrix (dashed black lines) and move radially outward (to the right), although often its poloidal speed is often larger than its radial speed. There were more blobs found within 1 msec in the Ohmic shot than in 2 msec for the H-mode shot, and almost no blobs detected inside the separatrix for the H-mode shot. The details of the blob motion are highly variable even within even these short time periods.

4.1 Blob radial profiles

Figure 9 shows radial profiles of blob statistics found using all shots in the database, sorted similarly to Fig. 3 in terms of H-mode, Ohmic, and L-mode plasmas. Each point includes all the blobs found within ±1 cm of that radial position (e.g. from -3 cm to -1 cm for the ρ= -2 cm zone). The time period is the same as for Fig. 3 (±5 msec

around the peak of the GPI signal), with error bars showing standard deviations over these shots.

The number of blobs detected per frame vs. radius is shown in Fig. 9(a), averaged over the ~4000 frames used for blob analysis for each shot. Very few blobs were identified inside or near the separatrix for H-mode plasmas; in fact, for 13/93 of these H-mode shots there were no blobs at all at $\rho = -2$ cm inside the separatrix. However, at 2 cm and 4 cm outside the separatrix the number of blobs per zone was similar for all types of shots. The normalized blob amplitude as shown in Fig. 9(b) generally increased from inside to outside the separatrix for all types of discharges, with the average amplitude just above the blob detection threshold of 1.5 inside the separatrix. The average blob amplitude in the far-SOL was ~2.5-3 for all types of shots.

The blob poloidal lengths (i.e. the size scale of the blobs in the poloidal direction) as shown in Fig. 9(c) did not vary significantly with radius, but these lengths were somewhat higher for H-mode than for Ohmic or L-mode, similar to the poloidal correlation lengths in Fig. 3(c). The radial blob lengths as shown in Fig. 9(d) were somewhat larger inside the separatrix for H-modes than for Ohmic or L-modes, also similar to the radial correlation lengths in Fig. 3(d). The blob poloidal speeds as shown in Fig. 9(e) were generally in the ion diamagnetic direction, except for an electron diamagnetic speed inside the separatrix for Ohmic plasmas, similar to Fig. 3(e). In the SOL, the blob poloidal velocities get closer to zero at larger radii, similar to the poloidal correlation velocity. The blob radial speeds are outward and generally lower than the poloidal speeds, and in the SOL the blob radial speeds increase at larger radii, both of which are similar to the radial cross-correlation speeds of Fig. 3(f).

4.2 Blob variations with global and local parameters

The blob database contains the six blob parameters of Fig. 9 for each of the 140 shots as a function of radius, along with the same global and local parameters used in Sec. 3. Note that each point in this database represents the average over hundreds of blobs for each shot, and not a single blob. Rather than repeat the entire statistical analysis of Sec. 3 for the blob database, we present just a few typical examples and then show in Sec. 4.4 that the blob results were similar to the correlation results.

Several examples of blob variations with the global and local parameters are shown in Fig. 10. The normalized blob amplitude shown in Fig. 10(a) decreases slightly with stored energy both inside and outside the separatrix, and is larger outside the separatrix than inside. The blob poloidal velocity in Fig. 10(b) shows a reversal with stored energy above ~100 kJ inside the separatrix, and a general trend for higher negative poloidal velocities for H-mode plasmas above 100 kJ. Similar trends are found with beam power and density since these are correlated with the stored energy.

Figures 10(c) and (d) show the variations of the blob poloidal length and radial blob velocity vs. the plasma current. There was little systematic variation of these blob

parameters with plasma current (or toroidal field) in this database, either inside or outside the separatrix. The blob radial velocity in the SOL tended to decrease with the line-averaged density (not shown). Figures 10(e) and (f) show the normalized blob amplitude and radial velocity as a function of the local electron temperature measured 2 cm inside the separatrix. There is a slight trend for decreased blob amplitude outside the separatrix with increasing temperature, and a slight trend of more negative blob radial velocity inside the separatrix at higher electron temperature. In general, variations in other blob properties were less clear than those shown in Figs. 10, i.e. there were few strong correlations between local blob properties and global or local parameters in this database, except for the blob L_{pol} with κ (see Table 6).

A separate attempt (not shown) was made to find clearer variations in blob scaling by evaluating the blob lifetime and the number of blobs over the whole GPI field of view, instead of using discrete radial zones. Over the entire database the average number of blobs/frame varied from ~0.15-1.5, and the average blob lifetime varied from ~15-50 μsec. However, there were no systematic variations in the number of blobs per frame or the average blob lifetime as a function of neutral beam power, plasma density, stored energy, plasma current, magnetic field, lithium coating, or any other global parameters in the database. Thus the blob formation and motion as defined here seems to be a generic or universal property of NSTX plasmas, at least in the SOL.

4.3 Relationships between blob properties

For the sake of completeness, we present some of the relationships among blob properties in Fig. 11. For this figure only the radial zones centered at ρ=0 cm and +2 cm are shown, since there are few blobs inside the separatrix for H-mode plasmas, and the main focus of blob physics is the SOL. Note again that each point represents the average of hundreds of blobs for each shot in each radial zone, and so the dynamics of individual blobs is not directly addressed in this database.

Figures 11(a) and (b) show that the radial blob velocity has little systematic variation with the normalized blob amplitude or poloidal blob length. Such variations might have been expected from analytic blob theory, as discussed in Sec. 6.4. Figure 11(c) shows the average blob V_{rad} vs. V_{pol} has a slight trend for increasing outward radial velocity with decreasing (negative) poloidal velocity (note that the positive V_{pol} blobs which appear at ρ= -2 cm in Fig. 10(b) do not appear at ρ=0 cm). Figure 11(d) shows the blob tilt angle with respect to the blob ellipticity, where a tilt angle of ~90º is vertical (i.e. poloidal), and ellipticity is defined as the ratio of the larger to smaller FWHM of the fitted blob ellipse. There seems to be a dominant clockwise tilt of ~10-30º from vertical for the measured ellipticities of 1-3. Figures 11(e) and 11(f) shows the ellipticity and tilt with respect to the *difference* in the average blob V_{pol} between the radial zones at +2 cm and 0 cm. There is no clear variation of ellipticity, but there is some correlation of the tilt in the 0 cm zone with this velocity difference (0.53 cross-correlation coefficient). This correlation might be related to the blob tilting with shear flow discussed in [17].

4.4 Comparison of blob properties with correlation properties

Some direct comparisons between blob properties and turbulence correlation properties are shown in Fig. 12. These properties are not expected to be identical due to the different analysis procedures, but it is interesting to know if the characterization of the turbulence is similar for the two methods.

Figure 12(a) shows that the normalized blob amplitude is quite well correlated with the δI/I (rms/mean) fluctuation level at both ρ =-2 cm and +2 cm, with linear cross-correlation coefficients of 0.84 and 0.70, respectively. Both the blob amplitude and the rms/mean are significantly smaller inside the separatrix, as also shown in Figs. 3 and 9. Figure 12(b) shows that the number of blobs generally increases with the rms/mean level, but with more scatter than for blob amplitude. Figure 12(c) shows the blob poloidal lengths (i.e. the blob size scales in the poloidal direction) are somewhat higher than the poloidal correlation lengths, but with a fairly high correlation between them at both ρ= -2 cm and +2 cm (0.60 and 0.72, respectively). Figure 12(d) shows that the blob radial lengths are close to the radial correlation lengths at ρ= +2 cm, but that the radial blob lengths are somewhat larger than the radial correlation lengths at ρ= -2 cm. Figure 12(e) shows that the blob poloidal velocity and the poloidal cross-correlation velocity are similar to each other at both radii, and that both properties show a change in direction at about W~100 kJ corresponding to the change from Ohmic to H-mode. Finally, Fig. 12(f) shows that the radial blob velocities are similar to the radial correlation velocities, with a predominantly outward radial velocity at both radii, but with a wide scatter (including some inward velocities) at ρ = -2 cm.

The results of the MLR analyses of the blob properties summarized at the bottom of Table 6 had only a partial similarity to the MLR analyses of the correlation properties at the top of Fig. 6, e.g. there were similar κ and lithium dependence of the correlation lengths, but dissimilar sensitivities to stored energy. Thus we can not assume that the blob properties and correlation properties have equivalent variations in this database.

5. Summary and discussion of results

Sections 5.1-5.4 summarize and discuss the variations which were observed for each type of fluctuation analyzed in Secs. 3 and 4. Section 5.5 provides a rough estimate of the transport implications of these fluctuations.

5.1 Fluctuation level variations

The radial variations of the relative GPI light fluctuation levels δI/I (rms/mean) in Fig. 3(a) and the blob amplitudes in Fig. 9(b) both show larger relative fluctuations in the SOL than just inside the separatrix. The relative fluctuation levels within ±2 cm of the separatrix are also significantly lower in H-mode compared to L-mode and Ohmic

plasmas. The most striking radial variation is the near-absence of blobs inside the separatrix in H-mode cases compared to Ohmic or L-mode, as shown in Fig. 9(a).

The parameter variations in fluctuation levels with global and edge plasma parameters were largely those associated with the changes occurring from Ohmic to H-mode plasmas. For example, the decrease in $\delta I/I$ with increasing line-averaged density in Fig. 4(a), and the decrease in $\delta I/I$ and blob amplitude with increasing edge temperature in Figs. 6(b) and 10(e), were mainly associated with the higher NBI power in H-mode. The decrease in edge fluctuations at the L-H transition is well known, but the present database does not contain the physics parameters which presumably control this transition (e.g. the edge flow shear).

The $\delta I/I$ also tended to decrease with increasing Li coating both inside and outside the separatrix, as shown in Fig. 4(b). Although this might be related to the reduced recycling due to lithium, there is also a fairly high (45%) correlation between increased lithium and higher density due to the frequent use of lithium in high-power H-mode discharges. In general, it was not possible to isolate a clear dependence of the fluctuation levels on a specific global parameter due to the co-dependency of the NBI power, stored energy, line-averaged density, and Li content with the H-mode in NSTX. The physics of these fluctuation levels is discussed further in Sec. 6.2.

It is worthwhile to note here the relationship between the GPI light fluctuations and the underlying density and/or temperature fluctuations. As discussed in Sec. 2.5, the relative light fluctuation levels will be dependent on the exponents relating the $D\alpha$ emission to the local electron density or temperature. The expected density exponent is $\alpha \sim 0.65$-0.80 for $\rho = -2$ cm and $\alpha \sim 0.7$-1.0 for the SOL. Therefore if the edge and SOL fluctuations were dominated by density fluctuations, the measured profiles of $\delta I/I$ of Fig. 3(a) and blob amplitudes in Fig. 9(b) should have a similar shape to the actual profiles of $\delta n/n$. However, some of the decrease in $\delta I/I$ from Ohmic to H-mode plasmas may be due to the decreased sensitivity of $\delta I/I$ to $\tilde{n}/n$ at higher density (e.g. from $\alpha = 0.80$ to 0.65), and the smaller response of $\delta I/I$ to $\delta n/n$ at higher densities may also reduce the number of blobs detected in H-mode cases in Fig. 9(a). These corrections could be made for specific cases in which the profiles are well known, such as Fig. 2, but can not be made when the fluctuation levels are large, since the instantaneous densities and temperatures are not measured. The effects of possible electron temperature fluctuations on the $\delta I/I$ profiles are less clear, since the magnitude of these fluctuations is not well known, but the sensitivity of $\delta I/I$ to $\delta T_e/T_e$ is generally less than that for $\delta n/n$, except below $T_e \sim 10$ eV. A similar difficulty with δT_e occurs in the interpretation of Langmuir probe fluctuations.

5.2 Length scale variations

The poloidal and radial correlation lengths were fairly constant vs. plasma radius, as estimated from both the turbulence in Figs. 3(c) and 3(d) and from the blob size in Fig. 9(c) and 9(d). There was up to a x2 increase in these size scales inside the separatrix, and in H-mode compared to Ohmic plasmas. Over the whole database, the poloidal size scale

of the turbulence was ~20-30% larger than the poloidal size scale of the blobs, as shown in Fig. 12(c), and the radial size scale of the turbulence was very similar to the radial blob size in the SOL, as shown in Fig. 12(d). However, inside the separatrix the radial size scale of the turbulence is up to ~2-3x larger than the radial size scale of the blobs, which suggests that the local cross-correlations overestimate the radial extent of the structures there. Note that the nonlinearity of δI with δn should not affect the size scales, as discussed in Sec. 2.5.

There was a slight decrease in L_{rad} with plasma current as illustrated in Figs. 4(e). However, there was a significantly higher L_{rad} with increased stored energy above the Ohmic-to-H-mode transition energy of W~100 kJ, as shown in Fig. 4(f). Table 3 also showed a moderately high correlation of both L_{pol} and L_{rad} with higher W, P_{NBI} and higher density, which all go along with the increase in stored energy during H-mode.

The radial and poloidal turbulence scales are within a factor of two of each other over nearly the whole database both inside and outside the separatrix, and a similar result was obtained for the blob scale lengths (not shown). The average ratio over the whole database was L_{pol}/L_{rad}=1.2±0.5 at ρ= -2 cm and L_{pol}/L_{rad}=1.5±0.4 at ρ= +2 cm, and for the blobs scales L_{pol}/L_{rad}=1.3±0.5 at ρ= -2 cm and 1.8±0.4 at ρ= +2 cm, which shows a very consistent pattern of structures slightly elongated in the poloidal direction. Some discussion of the physics of these scale lengths is in Sec. 6.1.

5.3 Velocity variations

Methods for evaluating the turbulence and blob velocities were described in Sec. 2.4. Note that these velocities are *not* the same as the local fluid velocities, since turbulence can propagate in the rest frame of the fluid. However, for large amplitude blobs in the SOL it is plausible (but not proven) that the turbulence and blob velocities measured in these experiments are close to the local fluid velocities, since the structures there are relatively isolated filaments of plasma.

The radial profiles of the turbulence V_{rad} and V_{pol} for the entire database were shown in Figs. 3(e) and 3(f), and were nearly the same as the blob velocities in Figs. 9(e) and 9(f). The poloidal velocities were in the ion diamagnetic drift direction at V_{pol}~0.5-3 km/sec, except for the Ohmic shots inside the separatrix in the electron diamagnetic drift direction. The ion diamagnetic velocity in the SOL is consistent with the expected sign of the radial electric field associated with the connection to the divertor sheath, and the reversal of direction for Ohmic plasmas may be due to ExB flow or drift wave propagation inside the separatrix (see Sec. 6.5). The radial velocities were all in the outward at V_{rad}~0.1-1 km/sec, as expected for plasma radial flow across the separatrix into the SOL. There was a slight trend for lower radial velocities in H-mode plasmas, but not much outside the error bars.

There was little systematic variation in the poloidal velocity of the turbulence or blobs with the plasma stored energy in NBI-heated H-mode plasmas (W≥100 kJ), either

inside or outside the separatrix, as shown in Figs. 4(c) and 10(b). This is surprising since the stored energy depends on the NBI power, which is co-directed in NSTX, and any strong toroidal edge rotation should (or could) cause a significant edge fluid flow velocity in the ion diamagnetic direction, since $B_{pol}/B_{tor} \sim 1$ at the edge of NSTX. Although the main ion fluid velocity was not measured, the edge CIII velocity did not have a NBI-dependent velocity in either the toroidal or poloidal direction, as shown in Fig. 7(a), and the toroidal CIII velocity was directed opposite the NBI direction. There was little or no change in the turbulence V_{pol} with the edge T_e or grad P_e, as shown in Figs. 6(e) and 6(f), which is surprising since the poloidal ExB velocity and wave phase speed should depend on these parameters. The physics of V_{pol} is discussed further in Sec. 6.3.

The radial velocity of the turbulence and blobs on the SOL is of special interest since it determines (at least in part) the width of the heat flux deposition on the divertor plates, and the heat load and impurity generation from midplane vessel structures. There was little or no variation of the turbulence or blob V_{rad} in the SOL with plasma current in this database, as shown in Figs. 4(e) and 10(d). There was also relatively little correlation of the turbulent V_{rad} with any global quantity in Table 3, or of the blob V_{rad} with the blob amplitude or blob L_{pol} in Figs. 10(a) and 10(b). Thus the physics of V_{rad} has not been clarified by this database, although some comparisons will be made with analytical blob model predictions in Sec. 6.4.

Finally, it is interesting to note that there is no clear relationship between V_{rad} and V_{pol} either for turbulence or blobs in the SOL, as shown in Figs. 4(b) and 11(c). Apparently the poloidal velocity of the turbulence and blobs in the SOL is independent of the radial velocity, with the $V_{pol} > V_{rad}$ for most cases.

5.4 Autocorrelation time variations

The radial profiles of τ_{auto} increased with radius from ~15 to ~40 μsec for Ohmic, L-mode, and H-mode plasmas, as shown in Fig. 3(b). Over the entire database, the autocorrelation time was fairly highly correlated with NBI power, stored energy, and line-average density, as shown in Table 3, but not correlated with I_p (or B_t). There was also a fairly high correlation between the autocorrelation time and the poloidal correlation length, as shown in Fig. 5(e), i.e. 73% at ρ= - 2 cm and 58% at ρ= +2 cm. The autocorrelation time is also highly correlated with the parameter L_{pol}/V_{pol}, as discussed in Sec. 3.3. Thus for example, the increase in τ_{auto} at ρ= +4 cm is mostly due to the decrease in V_{pol} there, as shown in Fig. 3(e).

The average blob lifetime was also evaluated from blob tracking over the entire imaging field of view, as illustrated by the sample blob tracks in Fig. 8. This average lifetime was 29±7 μsec over the whole database, which included hundreds of blobs for each shot. This is not much more than the average autocorrelation times of τ_{auto}=22±9 μsec at ρ= -2 cm and τ_{auto}=28±8 μsec at ρ= +2 cm, averaged over the whole database, in part since many blobs do not move far over the GPI field of view, as illustrated in Fig. 8.

5.5 Estimates of turbulent heat transport

The local electrostatic (conductive plus convective) heat transport due to edge turbulence is: $P = 5/2\langle \delta p\ \delta V_r \rangle$, where P is the power loss, δp are the local pressure fluctuations, $\delta V_r = \delta E_{pol} x B_t$ are the local radial velocity fluctuations, and brackets indicate the time-averaged cross-correlation [3]. Thus direct quantitative inferences about heat transport can not be made from GPI measurements, which do not provide any of the needed quantities; namely, the local density, temperature, or radial fluid velocity fluctuations (the turbulence velocity is not necessarily the same as the fluid velocity).

However, it possible to use the measured quantities to estimate a rough upper bound on the edge heat transport due to turbulence or blobs, and to see how this varies with the total power input. For this we assume that $T_i = T_e$ locally, i.e. $\delta p \sim 2\delta(nT_e)$, and that $\delta(nT_e)/nT_e \sim \delta I/I$ from GPI, i.e. the Dα light fluctuations exponents $\alpha+\beta \sim 1$ (see Sec. 2.5). Furthermore, we assume that the turbulent fluctuations in V_{rad} are equal to the time-averaged V_{rad} measured by GPI (a very rough assumption), and that these fluctuations are in phase with the density/temperature fluctuations given by $\delta I/I$. Finally, we assume that this local heat flux occurs over an area within about ±45º of the outer midplane, i.e. an area $A \sim 10^5$ cm^2, to estimate the total turbulence heat flux as $P_{turb} \sim 5\ nT_e\ (\delta I/I)\ V_{rad}\ A$.

Figure 13(a) shows this highly simplified estimate for P_{turb} evaluated at $\rho = -2$ cm for the whole database plotted as a function of the total power input $P_{tot} = P_{OH} + P_{RF} + P_{NBI}$, with the power ranges of Ohmic, L-mode, and H-mode plasmas shown at the bottom. Most of the increase in this estimated P_{turb} with P_{tot} is due to the increases in nT_e with P_{tot}, since $\delta I/I$ and V_{rad} do not increase with power. A linear fit to the data points is shown by the red line, and the blue line shows $P_{turb} = P_{tot}$. The linear fit suggests that (on average) P_{turb} increases with P_{tot}, and that about half the input power might be due to turbulent transport across the edge. However, this estimate of P_{turb} is clearly accurate to no better an order-of-magnitude due to the assumptions in the previous paragraph; for example, there are points above the blue line and below zero which are unphysical. The Ohmic shots with P_{tot} =0.5-1.5 MW almost all have a P_{turb} <0.5 MW, which is consistent with power balance. An appropriate inference from Fig. 13(a) might be that the power loss due to edge turbulence could explain a significant part of the total power loss for many of the shots in this database.

It is also possible to estimate the power loss due to blob transport across the separatrix under similarly rough assumptions. We assume that blobs are born near $\rho = -2$ cm and move radially outward with a constant energy across the separatrix into the SOL. The energy in an individual blob is taken to be $E_{blob} \sim 2nT_e * Amp * Vol_{blob}$ where n and T_e are the average density and electron temperature at $\rho = -2$ cm, $T_i = T_e$, Amp is the normalized amplitude of the blob above the background at $\rho = -2$ cm, and the blob volume is $Vol_{blob} \sim (2\pi R) L_{rad} * L_{pol}$, where L_{rad} and L_{pol} are the radial and poloidal correlation lengths of the blob at $\rho = -2$ cm. The mean blob energy over the database as defined this way is $E_{blob} \sim 100$ Joule. The frequency of blobs crossing the separatrix can be estimated as $f_{blob} \sim N_{blob} * (130\ cm/30\ cm) * (V_{rad}/2\ cm)$, assuming the blob number density within ±45º of the outer midplane is given by the observable N_{blob} number found within the 30

cm high poloidal GPI region in the ρ= 0 cm radial zone of Fig 9(a), and that the transit time across this 2 cm wide zone is (2 cm/V_{rad}), where V_{rad} is the blob radial velocity near ρ= 0 cm. The mean blob frequency crossing the separatrix is thus ~10^4 /sec. The total blob power loss is then estimated as $P_{blob} \sim E_{blob} f_{blob}$.

Figure 13(b) shows this highly simplified estimate for P_{blob} for the whole database plotted as a function of the total power input $P_{tot} = P_{OH} + P_{RF} + P_{NBI}$, with the power ranges of Ohmic, L-mode, and H-mode plasmas shown at the bottom. A linear fit to the data points are shown by the red line, and the blue line shows $P_{blob} = P_{tot}$. Most of the increase in this estimated P_{blob} with P_{tot} is again due to the increases in nT_e with P_{tot}, since the amplitude does not increase with power and V_{rad} is actually reduced in H-mode (Fig. 9). The linear fit suggests that (on average) P_{blob} increases with P_{tot}, and that about 1/6 of the input power might be accounted for as blob transport across the edge. However, this estimate of P_{blob} is clearly accurate to no better an order-of-magnitude due to the various simplified assumptions in the previous paragraph.

6. Relationships to theory and previous experiments

This section describes the relationship of the present results to relatively simple theoretical models for the turbulence scale lengths in Sec. 6.1, fluctuation levels in Sec. 6.2, poloidal velocity in Sec. 6.3, and radial blob velocity in Sec. 6.4. Section 6.5 contains a discussion of relationships with previous experimental results.

6.1 Turbulence scale length vs. theory

The theory of edge turbulence in tokamaks focuses on drift-waves and/or interchange modes driven by temperature and/or density gradients. Numerical evaluation of the nonlinear saturation of these instabilities has been done for several specific cases with large codes, for example in [17,21,22]. However, for a large database like this it not possible to compare the results with detailed turbulence simulations, but only with the general trends expected from simplified models for these instabilities.

Figure 14(a) shows a comparison of the poloidal turbulence scale lengths derived from the correlation analysis of Sec. 3 with the generic drift-wave model gyroradius parameter $\rho_s = 10^2(M_i T_e)^{1/2}/Z_i B_t$, where B_t is taken as the field at the magnetic axis. The L_{pol} scale lengths are the FWHM as measured 2 cm inside the separatrix. For the gyroradius scale we assume M_i=2 and Z_i=1 for the main deuterium ions and T_e measured by the Thomson scattering 2 cm inside the separatrix. Dashed lines are shown for two values of $k_{pol}\rho_s$, where we assume $k_{pol} = 2/L_{pol}$. The data in Fig. 14(a) are best fit by $k_{pol}\rho_s \sim 0.06$ (or $k_{pol}\rho_s \sim 0.12$ using the outer edge B), which corresponds to a poloidal scale length a few times larger than expected from usual linear drift-wave instabilities at $k_{pol}\rho_s \sim 0.3$. The larger size scales measured in H-mode shots are at least qualitatively consistent with the larger drift-wave gyroradius scale in those shots, although there is a factor-of-two scatter in $k_{pol}\rho_s$. Note that there can also be a significant component of

carbon ions in the region 2 cm inside the separatrix with M_i=6 and Z_i~2, which is not taken into account in this comparison.

The theory of interchange modes predicts a broad spectrum of instability up to the size scale of the pressure gradient scale length [23,24]. Figure 14(b) shows a comparison of the radial turbulence length L_{rad} derived from the correlation analysis of Sec. 3 with the pressure scale length L_p measured by Thomson scattering, both evaluated at 2 cm inside the separatrix. For Ohmic shots this relationship is L_{rad} ~(2-4)L_p, but for H-mode shots L_{rad}~(5-15)L_p. Thus the radial scale length of the turbulence in Ohmic plasmas at 2 cm inside the separatrix is similar to that expected from the interchange scale length, but for H-mode plasmas it is significantly larger than expected. This relationship could not be tested at larger radii since the local pressure gradient scale lengths were not well known there.

6.2 Turbulence fluctuation level vs. theory

The nonlinear saturation level expected for turbulent fluctuations due to the generic "wave-breaking" mechanism is $\delta n/n \sim 1/k_{rad}L_n$, independent of the type of linear instability. Figure 15(a) shows a test of this relationship at 2 cm inside the separatrix assuming $\delta I/I = \delta n/n$ (see below) and $k_{rad}=2/L_{rad}$, where L_{rad} is the radial scale length from correlation analysis. Most of the Ohmic and L-mode shots are near this wave-breaking limit with $\delta I/I \sim (0.5\text{-}1)L_{rad}/2L_n$. However, the measured fluctuation levels for the H-mode shots are $\delta I/I \sim (0.06\text{-}0.3)L_{rad}/2L_n$, i.e. much smaller than expected from the wave-breaking limit, and also apparently independent of L_{rad}/L_n. In other words, the expected radial scale lengths in H-mode plasmas are ~3-15 times those expected from the wave-breaking limit. This relationship could not be tested at larger radii since the local density gradient scale lengths were not well known.

A nonlinear saturation level for interchange turbulence is expected due to the radial convection of fluid motion, i.e. $\delta n/n = \delta V_{rad}/\omega L_n$, where ω is a typical frequency of the turbulence and δV_{rad} is the radial velocity fluctuation. Assuming that $\delta I/I = \delta n/n$, $\delta V_{rad} = V_{rad}$ (i.e. the fluctuating δV_{rad} is near its time-averaged value), and $\omega \sim 2/t_{auto}$, the database results for ρ= -2 cm are plotted in Fig. 15(b). The observed fluctuation levels mostly close to this limit in Ohmic plasmas, but smaller by a factor of ~2-8 in H-mode plasmas, at least qualitatively similar to the results of Fig. 15(a). However, in general L_{rad} is not well correlated with $V_{rad}\,\tau_{auto}$ so these two plots in Fig. 15 are not identical, and in some shots the measured V_{rad} is zero or negative, which is not at all consistent with this scaling.

Note that the relative fluctuation levels $\delta I/I$ used for Fig. 15 could be converted to $\delta n/n$ using the expected variation of the Dα light emission $\delta I/I = \alpha\, \delta n/n$, where α~0.65-0.80 for the range of n_e and T_e used for these plots (see Table 3). However, this would not significantly change the qualitative results, and would still leave unresolved the possible Dα dependence on δT_e, since the ratio $\delta T_e/\delta n$ is not known. Thus the results of Fig. 15 should be considered only an approximate or qualitative comparison of

experiment and theory. However, the large difference between the measured H-mode fluctuation levels and the x10 higher predictions from these models seems to be significant. This may in part be due to an overestimation of L_{rad} for H-mode cases, or perhaps the turbulence level in H-mode plasmas is determined by other physics such as the shear flow, which were not characterized in this database.

6.3 Turbulence poloidal velocity vs. theory

One interesting feature of these results is the change of the poloidal direction of the turbulence inside the separatrix from the electron diamagnetic (positive) direction for Ohmic plasmas to the ion diamagnetic (negative) for H-mode plasmas. In theory, the poloidal velocity of the turbulence is the sum of the turbulence velocity in the plasma rest frame plus the poloidal velocity of the plasma (e.g. due to toroidal rotation of field-aligned structures), both of which can be in either direction for various edge rotation and edge instabilities.

Figure 16 shows the poloidal velocity of the turbulence measured using the cross-correlation method vs. the calculated diamagnetic drift speed, both evaluated at 2 cm inside the separatrix. The diamagnetic drift speed is taken to be $V_{drift} = \pm c_s\rho_s/L_n$, where L_n is the density gradient scale length and ρ_s is evaluated using the magnetic field on axis. The Ohmic plasma have a velocity $V_{pol}\sim(1\text{-}3)V_{De}$, roughly consistent with an electron drift wave. However, the H-mode plasmas have $V_{pol}\sim(0.2\text{-}1)V_{Di}$, which is in the opposite direction and smaller than the ion diamagnetic velocity.

It seems plausible that the poloidal turbulence velocity in H-mode plasmas could be affected by edge poloidal plasma rotation. A toroidal plasma rotation in the direction of NBI should cause an apparent poloidal motion of field-aligned edge filaments in the negative (ion diamagnetic) direction with $V_{pol}(NBI) \sim (B_{pol}/B_{tor})V_{tor} \sim V_{tor}$, which is consistent with the direction of the observed turbulence V_{pol} in H-mode. However, the poloidal velocity of CIII near $\rho = -2$ cm was largely in the opposite direction, as shown in Fig. 7(b), the V_{tor} from the CIII data shows rotation in the opposite toroidal direction expected from NBI-induced rotation. On the other hand, edge poloidal velocities previously measured by charge exchange recombination spectroscopy in NSTX were positive in the sense of Fig. 16 [25], but these measurements were not available for the present database. Thus it not clear whether the CIII rotation data is representative of the plasma edge rotation in these experiments.

6.4 Blob radial velocity vs. theory

The formation rate of blobs near the separatrix and their radial velocity in the SOL may be important factors in determining the SOL width in present and future tokamaks. There are no simplified analytical models for the blob formation process, but there are simple models for the blob radial velocity which can be compared with this database.

Figure 17 shows a comparison of the measured radial blob velocity at 2 cm outside the separatrix with calculated blob velocities based on two different models [7]: with the sheath-limited velocity: $V_{sl} = c_s (L_{II}/R)(\rho_s/\delta_b)^2 (\delta n/n)$ in Fig. 17(a), and with the inertial range velocity: $V_{in} = c_s (\delta_b/R)^{1/2} (\delta n/n)^{1/2}$ in Fig. 17(b). For these plots c_s and ρ_s are the sound speed and drift-wave gyroradius evaluated within ±1 cm of the separatrix using T_e from Thomson scattering (using B on axis), L_{II} is the parallel connection length to the divertor, taken to be 4.5 meters with R=150 cm, δ_b is the blob radius, taken to be half the blob L_{pol} (FWHM) from the analysis of Sec. 4, and $\tilde{n}/n$ is taken to the normalized amplitude of the blobs at 2 cm outside the separatrix. Note that each point represent the average of hundreds of blobs identified for that radial region for that shot.

The measured radial blob velocities of V_{rad}~0.3±0.2 km/sec are generally higher than the calculated V_{sl} (which average ~0.1 km/sec), and lower than the calculated V_{in} (which average ~10 km/sec). This is consistent with the previous result that the SOL blobs in NSTX lie between these two regimes [14]. However, there does not appear to be any consistent variation of the measured velocities with these calculated velocities within this database.

6.5 Comparison with previous edge turbulence results

The first part of this section compares these GPI results with those of other edge turbulence diagnostics in NSTX. The later part of this section compares them with edge turbulence results from other machines.

In general, the results described in this paper are very similar to previous NSTX GPI results, including those done using HeI emission instead of Dα [9]. For example, fluctuation levels ~4 cm outside the separatrix in H-mode plasmas were near unity and independent of NBI power from ~2-6 MW, as shown in [11]. Somewhat higher poloidal velocities up to V_{pol}~8 km/sec were previously seen up to 5 cm inside the separatrix [10], a region not analyzed here. Note that the present database did not include cases where very small edge and SOL fluctuation levels were observed in Ohmic H-mode plasmas [11], or during the transient "quiet periods" seen just before the L-H transition [26].

Beam emission spectroscopy measurements of edge turbulence in the steep-gradient region of MHD-quiescent H-mode plasmas [27,28] showed poloidal correlation lengths of L_{pol} ~10-20 cm and correlation times of τ_{auto}~10-20 μsec, which are similar to the L_{pol} ~10 cm and τ_{auto}~25 μsec measured at ρ=-2 cm in H-modes in Fig. 3. The poloidal velocity of the turbulence seen in BES was V_{pol} ~ -5 km/sec, which is similar to the V_{pol} ~ -3 km/sec in Fig. 3. However, the relative fluctuation levels in BES were δn/n~1-5%, which is significantly smaller than the δI/I~15% in Fig. 3, and even farther from the δn/n~0.2-0.25 inferred for GPI results using the α exponent from Table 3. A detailed comparison of the BES and GPI measurements within the same discharges on NSTX will presented elsewhere [29]. Parameter scalings seen in this BES data included an increase in L_{pol} with dn/dr, and an increase in $\tilde{n}/n$ with dn/dr and $1/L_n$, whereas GPI

data for H-modes at ρ=-2 cm do not show significant trends in these directions, within the scatter in the data. However, the BES and GPI databases did not use the same discharges, and the global parameters and measurement locations are also different between these databases.

Measurements by microwave reflectometry ~1 cm inside the separatrix in NSTX [30] showed a decrease in edge density fluctuations from $\delta n/n$~20% to <1% with increased lithium coating, whereas the GPI fluctuation at ρ=-2 cm decreased from ~20% to ~10% (on average) with increased lithium coating, as shown in Fig. 4(b). Reflectometer measurements in the steep density gradient region between ELMs [31] were consistent with a radial correlation length of L_{rad}~2 cm (FWHM) and $\delta n/n$~1%, both of which are lower than the GPI measurements at ρ=-2 cm in ELM-free H-mode periods in Fig. 3. These differences between reflectometry and GPI are not yet understood. Langmuir probe measurements in L-modes and H-modes in NSTX [32] showed relative density fluctuation levels increasing from ~0.1 just inside the separatrix to ~0.5-1.0 in the SOL, similar to Fig. 3(a), and poloidal and radial correlation lengths of L_{pol}~4-9 cm and L_{rad}~2-6 cm, similar to Figs. 3(c) and 3(d). Radial blob speeds from the probe were ~ 1-4 km/sec in the SOL, somewhat higher than the results from Fig. 11(a)-11(c).

The results in the present paper are quite similar to edge turbulence measurement with a fast camera and probes on MAST, which is the machine most nearly like NSTX. For example, imaging of the edge blobs (a.k.a. filaments) in MAST showed lifetimes ~40-120 μsec, poloidal and radial widths L_{pol}~7-12 cm and L_{rad}~3-10 cm, and radial velocities V_{rad}~0.5-2 km/sec [33], all similar to the blobs characterized here in Figs. 9-12. Blobs in MAST were also seen to rotate toroidally in the co-current direction V_{tor}~5-12 km/sec, a measurement which was not available with the GPI diagnostic on NSTX. The relative fluctuation level in the ion saturation currents in Langmuir probes in MAST increased from ~0.4 at 1 cm inside the separatrix to ~0.8 at 4 cm outside the separatrix [34], similar to the GPI fluctuation levels in Fig. 3(a). These probe result also agreed at least qualitatively with numerical simulations of interchange instability done with the ESEL code, although possible effects of electron temperature fluctuations were noted.

The GPI diagnostic on Alcator C-Mod shows similar edge fluctuation levels, autocorrelation times, and turbulence velocities as NSTX [35], but has correlation lengths L_{pol}~L_{rad}~1 cm, which are about ten times smaller than NSTX, presumably due to the x10 higher toroidal field. The dual GPI diagnostic on EAST [36] was used study time-dependent velocities during dithering bursts prior to H-mode, and showed a reversal in the average V_{pol} direction across the separatrix, similar to that the Ohmic shots here in Fig. 3(e).

As noted in the Introduction, there have been several review papers covering edge turbulence in tokamaks, so many results in the present paper have been seen previously. For example, the increase in relative fluctuation level with minor radius across the separatrix is nearly universal [2,3], as is the poloidal size scaling $k_{pol}\rho_s$~0.02-0.1[4,5]. The reversal of the poloidal velocity vs. radius in Ohmic plasmas was first seen in TEXT [37]. Tokamak blob sizes ranged from ~0.5-4 cm (half-width) and radial velocities were

~0.2-3 km/sec [7] which are within or near the range shown in Fig. 9, and the radial blob velocities were bounded by the inertial and sheath-limited models, as they were in Fig. 17 here.

There have been several previous studies of edge turbulence scaling within a single tokamak. For example, the edge density fluctuation levels ñ/n did *not* vary with ρ_s/L_n or the local density at a fixed radius in Ohmic TEXT plasmas [38], similar to results here at ρ = -2 cm (not shown in the figures). In ASDEX Ohmic discharges [39], the poloidal correlation length increased and the poloidal velocity decreased with increased density, whereas here the L_{pol} at ρ= +2 cm and +4 cm decreased, and the V_{pol} increased, with density, opposite to ASDEX. In DIII-D [40] the relative density in blobs (a.k.a. "IPO's") normalized to the local plasma density in the SOL in L-mode plasmas was fairly constant vs. line-averaged density; here also the average blob amplitude at ρ= +2 cm and +4 cm was constant vs. plasma density over all regimes, to within the scatter. In Alcator C-Mod [41,42] the size of blobs measured by GPI in the SOL varied little with discharge parameters, similar to the present results, but the radial velocities increased with density, which is different from the present results.

The most recent study of blobs was done in the SOL of L-mode plasmas in ASDEX Upgrade using a 1-D (radial) lithum-BES diagnostic [43]. These blobs, as defined by a conditional sampling criterion, had radial size ~3-8 cm (FWMH), a mean outward radial velocity ~0-1 km/sec, and a relative fluctuation level $\delta I/I$ ~0.1-0.6, all of which are similar to the NSTX blob results of Sec. 5. The ASDEX Upgrade blob size and average radial velocity were almost constant with radius and their relative intensity (i.e. normalized blob amplitude) increased with radius, all similar to blobs in the NSTX SOL (Fig. 9). The ASDEX Upgrade blob properties did not vary significantly with the toroidal magnetic field, similar to the NSTX results.

A cross-machine database of seven tokamaks and stellarators was recently used to compare edge turbulence near the separatrix in L-mode plasmas [8]. The autocorrelation times and poloidal correlation lengths both inside and outside the separatrix were fit with power laws as $\tau_{auto} \sim (L_n/c_s)^{0.5\text{-}0.6}$ and $L_{pol} \sim \rho_s^{0.55}$. However, the present database showed little or no variation of τ_{auto} with L_n/c_s at ρ = -2 cm, but rather had $\tau_{auto}/(L_n/c_s)$ ~38 for L-mode plasmas, and the variation of L_{pol} with ρ_s as shown in Fig. 15(b) was fairly well fit by $L_{pol} \sim 33\rho_s$. Radial blob speeds from conditional averaging in [8] were outward and mainly within V_{rad}~0-3 km/sec, similar to the V_{rad}~0-1 km/sec of Fig. 9(f).

7. Conclusions

This paper described edge and SOL turbulence in NSTX using a large database which covered most of the operational range of the machine. The specific goals were to determine how the turbulence varied with the global and local plasma parameters, how the turbulence characteristics were related to each other, and how well these turbulence variations could be described by simplified theoretical models.

There were clear systematic variations in the turbulence with minor radius across the database; for example, with increased distance into the SOL the fluctuation levels and autocorrelation times increased, the poloidal velocities decreased and the radial velocities increased. The clearest parametric variations in the edge turbulence were correlated with the changes which occurred from Ohmic to H-mode plasmas; for example, a decrease in fluctuation levels, an increase in poloidal correlation lengths, and a change in the direction of V_{pol} inside separatrix. However, it was not possible to isolate a unique global or local variable which caused these variations, since several parameters varied together with these changes, e.g. neutral beam power, plasma stored energy, line-averaged density, lithium coating, and the density and temperature just inside the separatrix.

Some interesting relationships were found between turbulence quantities across the whole database. For example, the poloidal and radial correlation lengths were usually within a factor-of-two of each other, and the autocorrelation time was usually near the poloidal correlation length divided by the poloidal velocity. On the other hand, there was no clear relationship between the radial turbulence velocity and the poloidal turbulence velocity, or the radial turbulence velocity and the radial or poloidal correlation lengths. It was interesting that the fluctuation levels, correlation lengths, and turbulence velocities found from correlation analysis were generally similar to those found from blob analysis.

With respect to the simplified theoretical models, the poloidal scale lengths were fairly well described by $k_{pol}\rho_s \sim 0.06$ (using the B on axis), which at least qualitatively explains the larger scale lengths in H-mode (i.e. hotter) plasmas. The relative fluctuation levels in Ohmic and L-mode plasmas were close to the wave breaking limit $\delta n/n \sim 1/k_{rad}L_n \sim 0.2\text{-}0.4$, but considerably lower than this limit in H-mode plasmas. The poloidal velocities were close to the electron diamagnetic drift speed in Ohmic plasmas, but considerable less than the ion diamagnetic speed in H-mode plasmas. The blob speeds at 2 cm outside the separatrix were were found to lie between the 'sheath limited' and 'inertial' range speeds, as previously found in NSTX and elsewhere.

There were several new and/or surprising results with respect to previous studies of edge turbulence. For example, there was no significant increase in the poloidal turbulence velocity with increased NBI power over $P_{nb} \sim 2\text{-}6$ MW in H-mode plasmas, despite increases in edge pressure and core toroidal rotation with NBI. The local radial correlation lengths just inside the separatrix in H-mode plasmas were ~2-5 times larger than the local density gradient scale, which seems inconsistent with drift wave theory. There was relatively little variation of the turbulence or blob properties with respect to plasma current or toroidal field, although the MLR analysis did indicate a significant increase in L_{pol} with κ, and a decrease in L_{pol} with I_p inside the separatrix. Although not new, there was a surprisingly clear reversal in poloidal turbulence velocity with radius in Ohmic plasmas, and the almost complete absence of blobs inside the separatrix for H-mode plasma.

We close by pointing out some uncertainties and limitations in the present results which could motivate further work. A major limitation is the lack of density and temperature data in the SOL, which makes make connections with turbulence theory

difficult. Ideally, the 2-D profiles of n_e and T_e should be measured on the timescale of the turbulence, so that the relationship between δn and δT_e determined. It would be interesting to correlate the edge turbulence variations with the edge impurity content, SOL flows, and heat flux width at the divertor plate. Turbulence measurements at other poloidal locations and better cross-diagnostic comparisons of the edge turbulence are also needed.

The present NSTX database was based on many separate experiments done during 2010, rather than on a small set of systematic parameter scans. This introduced uncontrolled variations in the edge neutral density, impurity levels, and magnetic geometry, so it was difficult to isolate clear parametric dependences in these results. With more systematic scans it might be possible to clarify the effects of parameters such as the plasma current, X-point location, lithium coating, or local gradients on the edge and SOL turbulence.

Finally, the data analysis procedures were kept simple for this large database, and there is still more to learn about the turbulence structure and motion than found in these scale lengths, fluctuation levels, and turbulence velocities. For example, further analysis could study the (ω,k) spectra, search for zonal flows and counter-propagating waves, identify blob formation, and study the nonlinear couplings in this turbulence.

Acknowledgments: We thank A. Dimits, D.A. D'Ippolito, and D.A. Russell for discussions, and J.-W. Ahn, D. Battaglia, J. Boedo, J. Canik, A. Diallo, S. Kubota, R. Maingi, J. Menard, D. Smith, V. Soukhanvoski for doing GPI gas puffs during their experiments. This work was supported by USDOE Contract DE-AC02-09CH11466.

References:

[1] Sabbagh S.A. et al 2014 Nucl. Fusion **53** 104007
[2] Surko C.M. and Slusher R.M. 1983 Science **221** 817
[3] Liewer P.C. 1985 Nucl. Fus. **25** 543
[4] Wootton A.J et al 1990 Phys. Fluids **B2** 2879
[5] Zweben S.J. et al 2007 Plasma Phys. Control. Fusion **49**, S1
[6] Boedo, J. 2009 J. Nucl. Mat. **390-391**, 29
[7] D'Ippolito D.A. et al 2011 Phys. Plasmas **18**, 060501
[8] Simon P. et al 2014 Plasma Phys. Control. Fusion **56** 095015
[9] Zweben S.J. et al 2004 Nucl. Fusion **44**, 134
[10] Zweben S.J. et al 2006 Phys. Plasmas **13** 056114
[11] Maqueda R.J. et al 2011 J. Nucl. Mat. **415**, S459
[12] Cao B. et al 2012 Plasma Phys. Cont. Fusion **54**, 112001
[13] Zweben S.J. et al 2014 Plasma Phys. Cont. Fusion **56**, 095010
[14] Myra J.R. et al 2006 Phys. Plasmas **13** 092509
[15] Myra J.R. et al 2011 Phys. Plasmas **18** 012305
[16] Russell D.A. et al 2011 Phys. Plasmas **18** 022306
[17] Myra J.R. et al 2013 Nucl. Fusion **53** 073013
[18] Cao B et al 2013 Fusion Sci. Tech. **64**, 29
[19] Davis W.M. et al 2014 Fusion Eng. Design **89** 717
[20] Stotler D.P. et al 2003 J. Nucl. Mat. **313-316** 1066
[21] Zweben S.J. et al 2009 Phys. Plasmas **16** 082505
[22] Halpern F. et al 2015 to be published in Plasma Phys. and Control. Fusion
[23] Myra J.R. et al 2008 Phys. Plasmas **15** 032304
[24] Scott B.D. 2005 Phys. Plasmas **12** 062314
[25] Bell R. et al 2010 Phys. Plasmas **17** 082507
[26] Zweben S.J. et al 2010 Phys. Plasmas 17 102502
[27] Smith D.R. et al 2013 Phys. Plasmas **20** 055903
[28] Smith et al 2013 Nucl. Fusion **53** 113029
[29] Sechrest Y. et al, to be submitted 2015
[30] Canik J.M. et al 2011 Phys. Plasmas **18** 056118
[31] Diallo A. et al 2013 Phys. Plasmas **20** 012505
[32] Boedo J.A. et al 2014 Phys. Plasmas **21** 042309
[33] Ben Ayed N. et al 2009 Plasma Phys. Cont. Fusion **51** 035016
[34] Militello F et al 2013 Plasma Phys. Cont. Fusion **55** 025005
[35] Terry J.L. et al 2007 Fusion Sci. Tech. 342
[36] Shao L.M. et al 2013 Plasma Phys. Control. Fusion **55** 105006
[37] Ritz Ch. et al 1984 Phys. Fluids **27**, 2956
[38] Rhodes T.L. et al 1993 Nucl. Fusion **33** 1147
[39] Endler M. et al 1995 Nucl. Fusion **35** 1307
[40] Boedo J.A. et al 2003 Phys. Plasmas **10**,1670
[41] Agostini, M. et al 2011 Nucl. Fusion **51** 053020
[42] Kube R. et al 2013 J. Nucl. Mat. **438** S505
[43] Birkenmeier G. et al 2014 Plasma Phys. Cont. Fusion **56** 075019

Table 1: Overall database parameters

Number of shots	140
Plasma current:	I_p=0.65-1.15 MA
Toroidal field:	B_t=3.5-5.5 kG
safety factor:	q_{95} = 5.8-12.8
Elongation	κ=1.9-2.5
Stored energy:	W_{mhd}=26-306 kJ
Average density:	n_e=1.3-7.0x10^{13} cm^{-3}
NBI heating:	P_{nb} = 0-6 MW
RF heating:	P_{rf} = 0-1.4 MW
Outer gap:	2.8-15.7 cm
Lithium:	0-370 mg/shot

Table 2: Sample plasma parameters

	H-mode	Ohmic
shot range	140389-395	141746-756
time (sec)	0.532	0.215
I_p (kA)	830	830
B_t (kG)	4.9	3.6
W_{mhd} (kJ)	220	32
n_e (10^{13} cm^{-3})	5.2	1.6
P_{nb} (MW)	4.0	0
$T_e(0)$ (eV)	920	530
$n_e(0)$ (10^{13} cm^{-3})	5.6	2.3
$T_e(a)$ (eV)	29±17	13±6
$n_e(a)$ (10^{13} cm^{-3})	0.92±0.54	0.37±0.23
T_e @ -2 cm (eV)	134±53	23±4
n_e @ -2 cm (10^{13} cm^{-3})	2.1±0.47	0.47±0.17
ρ_s (cm) @ -2 cm	0.3	0.2
τ_{ei} (μsec) @ -2 cm	1.5	0.5
β_e @ -2 cm	0.005	0.0003

Table 3: Average edge parameters at ρ= -2 cm vs. shot type and Dα exponents

shot type	shots	NBI+RF (MW)	T_e@-2cm (eV)	n_e@-2cm (10^{13} cm^{-3})	α exponent (for n_e)	β exponent (for T_e)
Ohmic	33	0	25±8	0.57±0.18	0.80±0.05	0.6±0.2
L-mode	14	0.8	34±17	0.87±0.42	0.75±0.05	0.4±0.2
H-mode	93	3.5	122±72	2.5±1.4	0.65±0.10	0.1±0.2

Table 4: Linear cross-correlation coefficients (red and italics for > 0.5).

	radius	I_p	B_t	P_{nb}	W_{mhd}	n_e-ave	Li/sh	edge n_e	κ	V_{tor}(C)
$\delta I/I$	-2 cm	0.01	*0.53*	*0.57*	*0.63*	*0.69*	0.44	*0.62*	0.36	0.28
	+2 cm	0.07	0.40	*0.66*	*0.63*	*0.63*	*0.54*	*0.64*	0.31	0.20
τ_{auto}	-2 cm	0.01	0.26	*0.61*	*0.60*	*0.65*	0.35	0.47	0.44	0.31
	+2 cm	0.23	0.16	0.35	0.43	0.36	0.31	0.27	0.39	0.21
L_{pol}	-2 cm	0.09	0.31	*0.65*	*0.65*	*0.61*	*0.52*	*0.55*	*0.53*	0.40
	+2 cm	0.02	0.21	0.45	*0.54*	0.46	*0.51*	0.28	*0.55*	0.40
L_{rad}	-2 cm	0.27	0.20	0.42	0.42	*0.54*	0.45	*0.61*	0.09	0.32
	+2 cm	0.24	0.14	0.06	0.02	0.16	0.38	0.14	0.31	0.16
V_{pol}	-2 cm	0.01	0.46	*0.63*	*0.69*	*0.68*	*0.59*	*0.53*	0.50	0.36
	+2 cm	0.18	0.05	0.04	0.08	0.11	0.19	0.29	0.10	0.24
V_{rad}	-2 cm	0.23	0.17	0.02	0.02	0.02	0.07	0.04	0.01	0.03
	+2 cm	0.20	0.31	0.40	0.44	0.36	0.34	0.33	0.41	0.03

Table 5: Power law exponents for linear cross-correlations > 0.5

	radius	B_t	n_e(ave)	edge n_e	W_{mhd}	Li/shot	kappa
$\delta I/I$	-2 cm	-1.7	-0.52	-0.30	-0.32	-	-
	+2 cm	-	-0.61	-0.37	-0.39	-0.11	-
τ_{auto}	-2 cm	-	0.62	-	0.39	-	-
	+2 cm	-	-	-	-	-	-
L_{pol}	-2 cm	-	0.55	0.29	0.37	0.09	2.9
	+2 cm	-	-	-	0.23	-	2.4
L_{rad}	-2 cm	-	0.64	0.36	-	-	-
	+2 cm	-	-	-	-	-	-

Table 6: Multiple linear regression exponents for correlations (top) and blobs (bottom)

	radius	I_p	B_t	n_e(ave)	Li/shot	W	kappa	edge n_e	dn_e/dR	q_{sep}	V_{tor}(C)
δI/I	-2 cm	-	*-0.88*	-0.19	-0.02	-	-	-	*-0.15*	-	-
	+2 cm	0.56	-	*-0.22*	-0.05	-	-	-	-	-	0.12
τ_{auto}	-2 cm	-	-	*0.45*	-	-	0.87	-	0.12	0.17	-
	+2 cm	*0.97*	0.68	*0.41*	-0.03	-	*-*	-0.13	-	0.23	-
L_{pol}	-2 cm	*-0.62*	-0.54	-	-	0.17	*1.43*	0.08	0.14	-	0.07
	+2 cm	-	*-0.80*	-	-	-	*1.52*	-	-	0.20	-
L_{rad}	-2 cm	-0.81	-	-	*0.08*	0.30	-1.60	-	-0.22	-	*0.15*
	+2 cm	-0.41	-0.52	-	*0.04*	*0.25*	*1.73*	-0.08	*0.17*	-	-
N	-2 cm	1.35	-	-	-	-	-3.70	-	-0.58	0.13	-
blob	+2 cm	-	1.35	-	-	-	*2.37*	-	0.03	-	-
A	-2 cm	-	*-0.15*	-	*-0.01*	0.03	-0.17	*-0.03*	-0.03	-0.03	-
blob	+2 cm	-	-		*-0.04*	-	*-*	*-0.15*	-	-	*0.11*
L_{pol}	-2 cm	-0.54	-	-	-	-	*1.63*	-	0.12	0.21	-
blob	+2 cm	-	-	-	0.01	-	*0.66*	-	-	0.09	-
L_{rad}	-2 cm	-	-	-	*0.05*	-	1.07	-	-	-	-
blob	+2 cm	-	-0.30	-	*0.16*	-	-	-0.04	-0.06	-	-

Figure Captions

1. Sample images of the normalized GPI Dα light emission vs. time for a typical H-mode shot during 4 MW of NBI (#140395). The time between these images is 10 μsec (4 frames) and their size is ~30 cm poloidally (vertical) x 24 cm radial (horizontal). Each image is normalized to the time-averaged image, and the relative fluctuation levels are shown by the color scale on the right. The location of blobs (defined in the text) is shown by the elliptical regions. The magnetic separatrix is the dashed line and the shadow of the limiter (RF antenna) is the dotted line.

2. Measured Thomson scattering data for the (a) electron temperature and (b) density for two sub-sets of this dataset: one Ohmic group and one H-mode group with 4 MW of NBI. Each plot contains data from 7 similar shots with the parameters defined in Table 2. Overlaid with the Thomson data is the radial profile of the GPI Dα light emission for these cases (same in both panels). All curves are plotted with respect to the separatrix as determined from the EFIT equilibrium reconstruction code. In (c) and (d) are typical GPI frequency spectra for these cases at radii $\rho = \pm$ 2 cm with respect to the separatrix.

3. Radial profiles of the turbulence correlation analysis for the entire database, grouped according to whether the shots were H-mode (93 shots), Ohmic (33 shots), or L-mode (14 shots). In (a) are the radial profiles of the relative GPI fluctuation levels δI/I (rms/mean), in (b) are the autocorrelation times τ_{auto} (FWHM), in (c) and (d) are the poloidal and radial correlation lengths L_{pol} and L_{rad} (FWHM) in cm, and in (e) and (f) are the poloidal and radial turbulence velocities V_{pol} and V_{rad} in km/sec. The error bars show the standard deviations over the shots in each group.

4. Several relationships between turbulence cross-correlation analysis and global plasma quantities over the entire database, plotted only at radii ρ= -2 cm and +2 cm for clarity. In (a) and (b) are the relative fluctuation level vs. the line averaged density and applied lithium per shot; in (c) and (d) are the turbulence poloidal velocity vs. the total stored energy and NBI power; in (e) and (f) are the radial correlation length vs. the plasma current and stored energy. The approximate divisions between Ohmic, L-mode and H-mode plasmas are shown where possible.

5. Relationships between various turbulence quantities over the entire database for radii ρ= -2 cm and +2 cm. In (a) are the radial vs. poloidal correlation lengths, in (b) are the radial vs. poloidal turbulence velocities, and in (c) and (d) are the radial turbulence velocity vs. the radial correlation length and relative fluctuation level, respectively. Part (e) shows the poloidal correlation lengths vs. the autocorrelation times, and part (f) shows the timescale for poloidal motion of turbulent structures vs. the autocorrelation time.

6. Relationships between edge plasma parameters and turbulence correlation quantities over the entire database. Part (a) shows the electron temperature vs. electron density at ρ= -2 cm, (b) shows these n_e and T_e vs. NBI power, (c) and (d) are the relative fluctuation levels vs. the edge T_e and ∇T_e and (e) and (f) are the poloidal velocities vs. the local T_e

and ∇P_e, respectively. The approximate divisions between Ohmic, L-mode and H-mode plasmas are shown where possible.

7. Relationship between the edge rotation diagnostic data and the turbulence poloidal velocity over the entire database. In (a) are the toroidal and poloidal CIII velocities vs. the applied NBI power. In (b) are the the toroidal and poloidal CIII velocities vs. the turbulence poloidal velocity at ρ= -2 cm. The red dashed line in (b) shows where the CIII velocity would equal the measured poloidal turbulence velocity.

8. Typical blob tracking results for an (a) Ohmic shot and (b) H-mode shot (141746 and 140395, respectively). The colored lines show all blob tracks for a 1 msec time period for the Ohmic shot and a 2 msec time period for the H-mode shot. The small ellipses show the blob shape and location at its starting time. The dashed line is the separatrix and the dotted line is the limiter shadow, and the image size is the same as in Fig. 1. The blob motion is highly variable in this radial vs. poloidal plane.

9. Radial profiles of blob statistics for all shots in the database, sorted according to shot type. In (a) is the average number of blobs per frame, which is significantly lower for H-modes inside or near the separatrix. In (b) is the normalized blob amplitude, where the minimum amplitude for tracking a blob is 1.5 in these units. In (c) and (d) are the poloidal and radial blob scale lengths, and in (e) and (f) are the poloidal and radial blob velocities.

10. Variation of blob properties with some of the global and local parameters in the database. The normalized blob amplitude in (a) decreases slightly with stored energy, and the blob poloidal velocity in (b) shows a reversal inside the separatrix at W~100 kJ. Parts (c) and (d) show the variations of the blob poloidal length and radial blob velocity vs. the plasma current, and (e) and (f) show the normalized blob amplitude and radial velocity as a function of the local electron temperature measured 2 cm inside the separatrix. The approximate divisions between Ohmic, L-mode and H-mode plasmas are shown where possible.

11. Some relationships between two blob properties at ρ=0 cm and +2 cm. Parts (a) and (b) show that the radial blob velocity has little variation with the normalized blob amplitude or poloidal blob length. Part (c) shows the average blob V_{rad} vs. V_{pol}, which shows a slight trend for increasing radial velocity with decreasing poloidal velocity. Part (d) shows the blob tilt angle with respect to the blob ellipticity, and parts (e) and (f) show the ellipticity and tilt variations with respect to the difference in average blob V_{pol} between the radial zones at +2 cm and 0 cm.

12. Comparisons between blob properties and cross-correlation properties at ρ=-2 cm and +2 cm. Parts (a) and (b) show that the normalized blob amplitude and the number of blobs are fairly well correlated with the cross-correlation $\delta I/I$ (rms/mean) fluctuation level. Parts (c) and (d) show a fairly high correlation between blob lengths and correlation lengths in both the poloidal and radial directions. Part (e) shows that the blob poloidal velocity and the poloidal cross-correlation velocity are similar to each other at

both radii, and (f) shows that the radial blob velocities are similar to the radial correlation velocities, with a predominantly outward radial velocity at ρ = +2 cm for both, and a wide scatter in both for ρ = -2 cm.

13. In (a) is the estimated edge power loss due to the measured turbulence P_{turb}, and in (b) is the estimated edge power loss due to the measured blobs P_{blob}, both plotted as a function of the total input power to the plasma P_{tot}. Each point corresponds to one shot in the database. Linear fits to the data are shown by the red lines, and the blue lines show $P_{turb}=P_{tot}$ or $P_{blob}=P_{tot}$. These results suggests that (on average) P_{turb} and P_{blob} increase with P_{tot}, and that a non-negligible fraction of the input power can be accounted for as turbulent or blob transport across the edge. The shaded bars at the bottom show the ranges of Ohmic, L-mode and H-mode plasmas.

14. Comparison of the measured length scales of the turbulence at ρ= -2 cm with simplified theoretical models. In (a) the poloidal correlation lengths L_{pol} are compared with the drift-wave gryoradius parameter ρ_s, showing a best fit to $k_{pol}\,\rho_s \sim 0.06$ (using the magnetic field on axis for B). In (b) the measured radial correlation lengths L_{rad} at ρ= -2 cm are compared with the radial pressure gradient scale length L_p, which is a scale expected from interchange turbulence. The best fits are $L_{rad} \sim 3\ L_p$ for Ohmic and L-mode plasmas and $L_{rad} \sim 10\ L_p$ for H-mode plasmas, which is significantly larger than expected for interchange modes.

15. Comparison of the measured fluctuation levels $\delta I/I$ at ρ= -2 cm with simplified theoretical models. Part (a) shows that Ohmic and L-mode shots are near the expected wave-breaking limit of $\delta I/I \sim L_{rad}/2L_n$, but H-mode shots are well below this limit. Part (b) shows that the Ohmic and L-mode fluctuation levels are generally near the expected interchange limit $\delta I/I \sim V_{rad}\,\tau_{auto}/2L_n$, but H-mode shots are well below this limit.

16. Comparison of the poloidal velocity of the turbulence measured using the cross-correlation method vs. the calculated diamagnetic drift speed, both evaluated at ρ= -2 cm. The diamagnetic drift speed is $V_{drift} = \pm\, c_s\rho_s/L_n$, where L_n is the density gradient scale length and ρ_s is evaluated using B on axis. The Ohmic plasma have a velocity $V_{pol}\sim(1\text{-}3)V_{De}$, which is roughly consistent with an electron drift wave. However, the H-mode plasmas have $V_{pol}\sim (0.2\text{-}1)V_{Di}$, which is smaller than the ion diamagnetic velocity.

17. Comparison of the measured radial blob velocity at 2 cm outside the separatrix with calculated blob velocities based on two different models: (a) the sheath-limited velocity: $V_{sl} = c_s\,(L_{II}/R)(\rho_s/\delta_b)^2\,(\delta n/n)$, and (b) the inertial range velocity: $V_{in} = c_s\,(\delta_b/R)^{1/2}\,(\delta n/n)^{1/2}$, using B on axis for ρ_s. Each point represent the average of hundreds of blobs identified for this radial region for a that particular shot. Almost all blob velocities lie between these two model velocities.

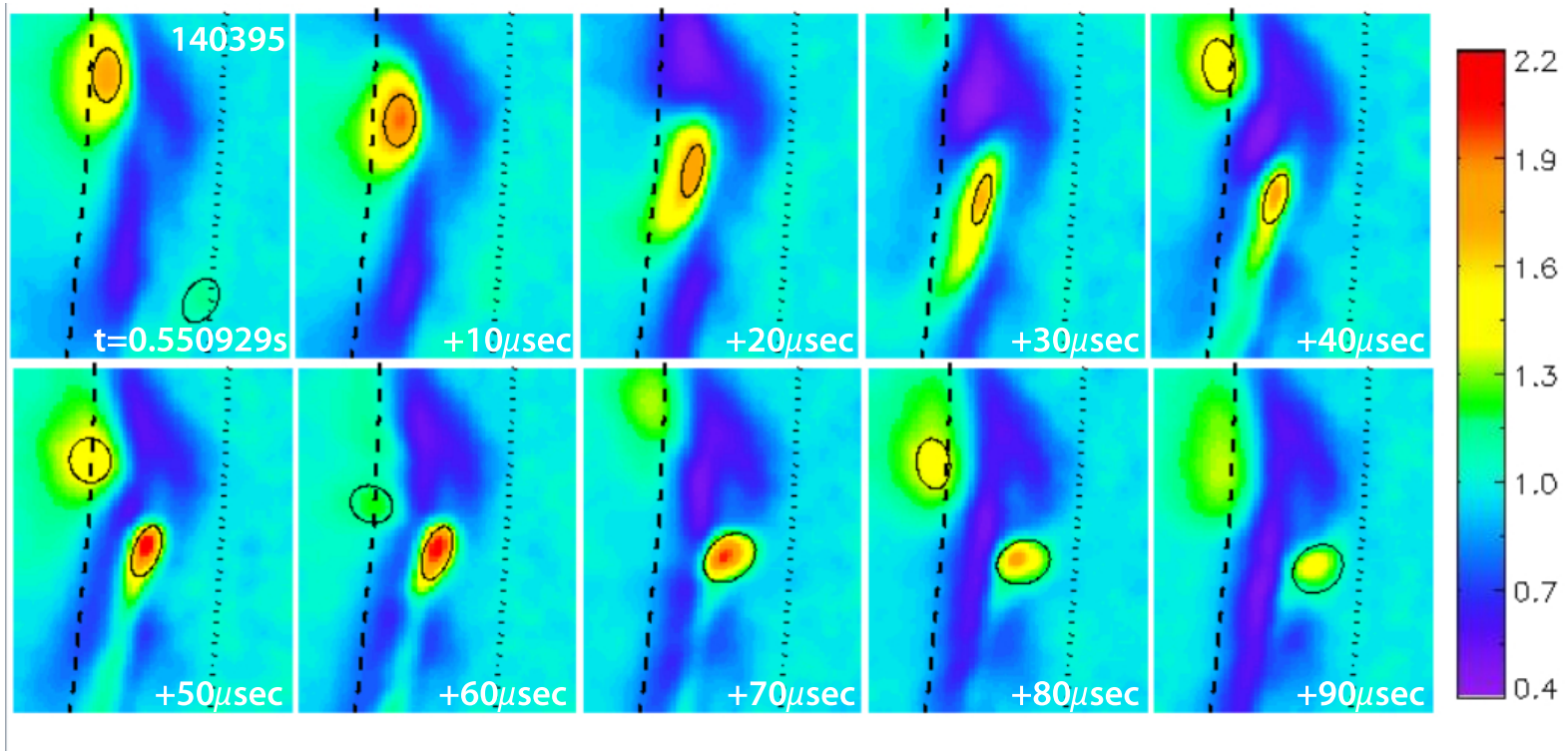
140395
t=0.550929s
+10μsec
+20μsec
+30μsec
+40μsec
+50μsec
+60μsec
+70μsec
+80μsec
+90μsec
2.2
1.9
1.6
1.3
1.0
0.7
0.4

Fig. 1

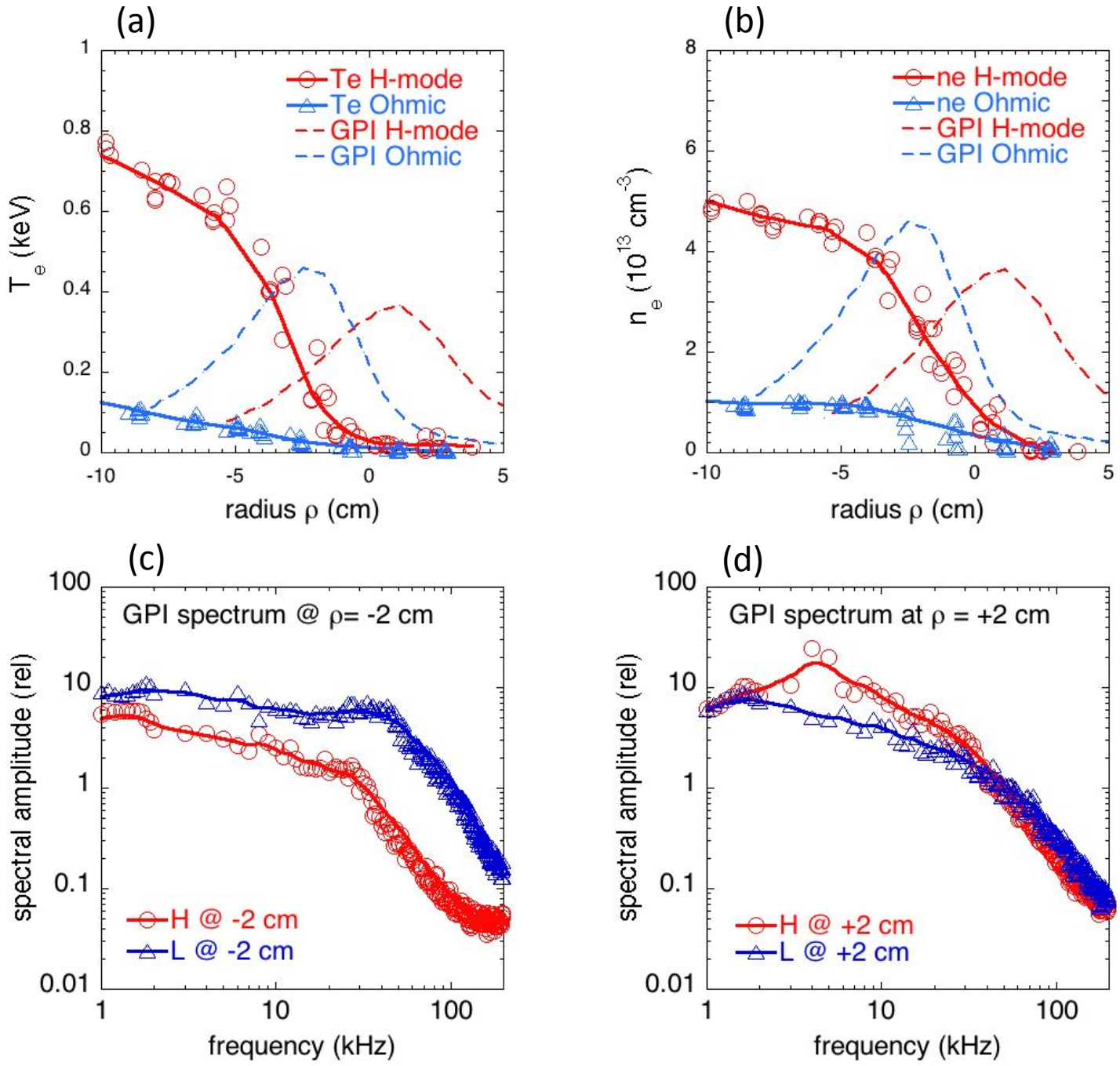
(a)
Te H-mode
Te Ohmic
GPI H-mode
GPI Ohmic
T_e (keV)
radius ρ (cm)
(b)
ne H-mode
ne Ohmic
GPI H-mode
GPI Ohmic
n_e (10^13 cm^-3)
radius ρ (cm)
(c)
GPI spectrum @ ρ= -2 cm
H @ -2 cm
L @ -2 cm
spectral amplitude (rel)
frequency (kHz)
(d)
GPI spectrum at ρ = +2 cm
H @ +2 cm
L @ +2 cm
spectral amplitude (rel)
frequency (kHz)

Fig. 2

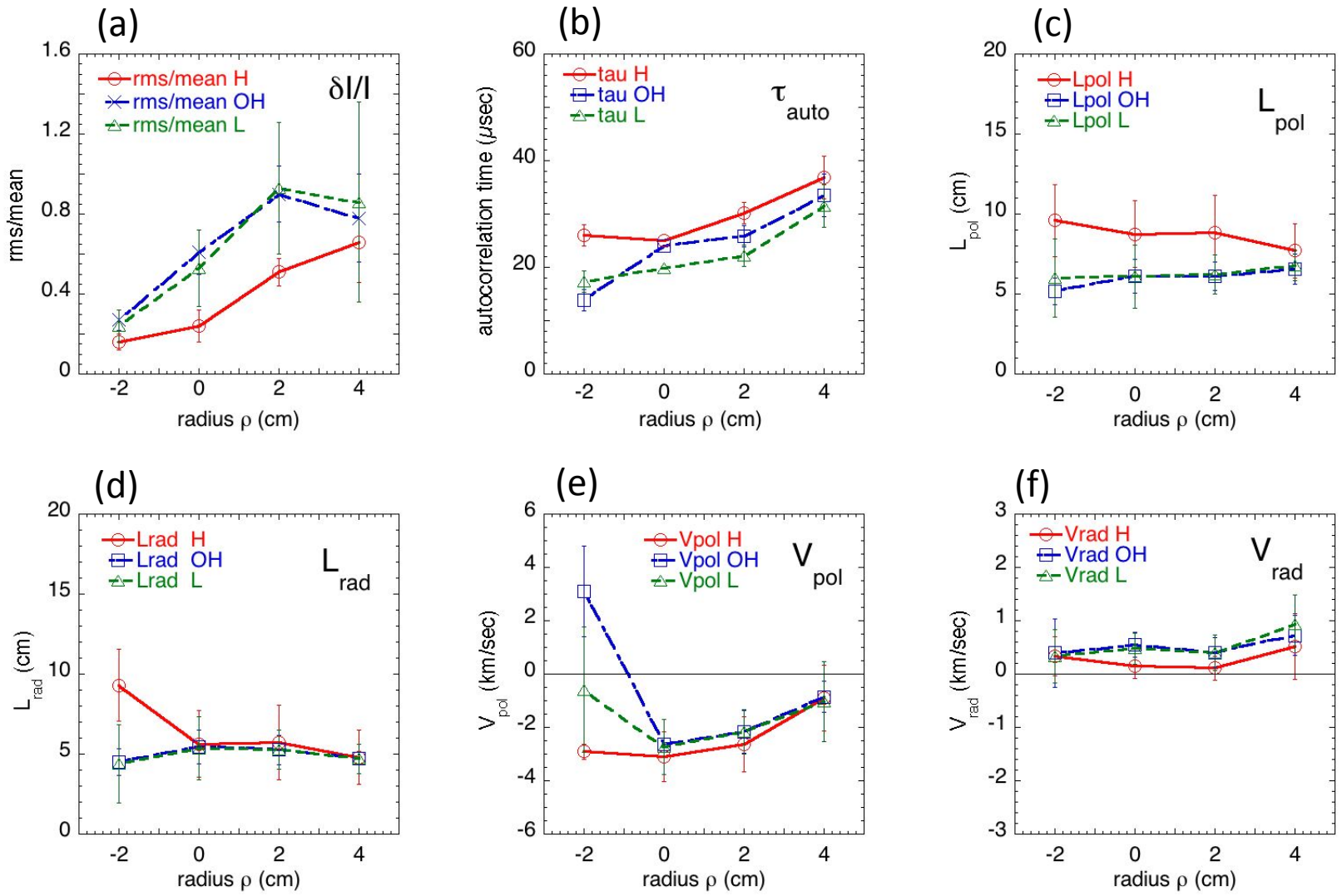
(a)
rms/mean H
rms/mean OH
rms/mean L
δI/I
rms/mean
radius ρ (cm)
(b)
tau H
tau OH
tau L
τ auto
autocorrelation time (μsec)
radius ρ (cm)
(c)
Lpol H
Lpol OH
Lpol L
L pol
L pol (cm)
radius ρ (cm)
(d)
Lrad H
Lrad OH
Lrad L
L rad
L rad (cm)
radius ρ (cm)
(e)
Vpol H
Vpol OH
Vpol L
V pol
V pol (km/sec)
radius ρ (cm)
(f)
Vrad H
Vrad OH
Vrad L
V rad
V rad (km/sec)
radius ρ (cm)

Fig. 3

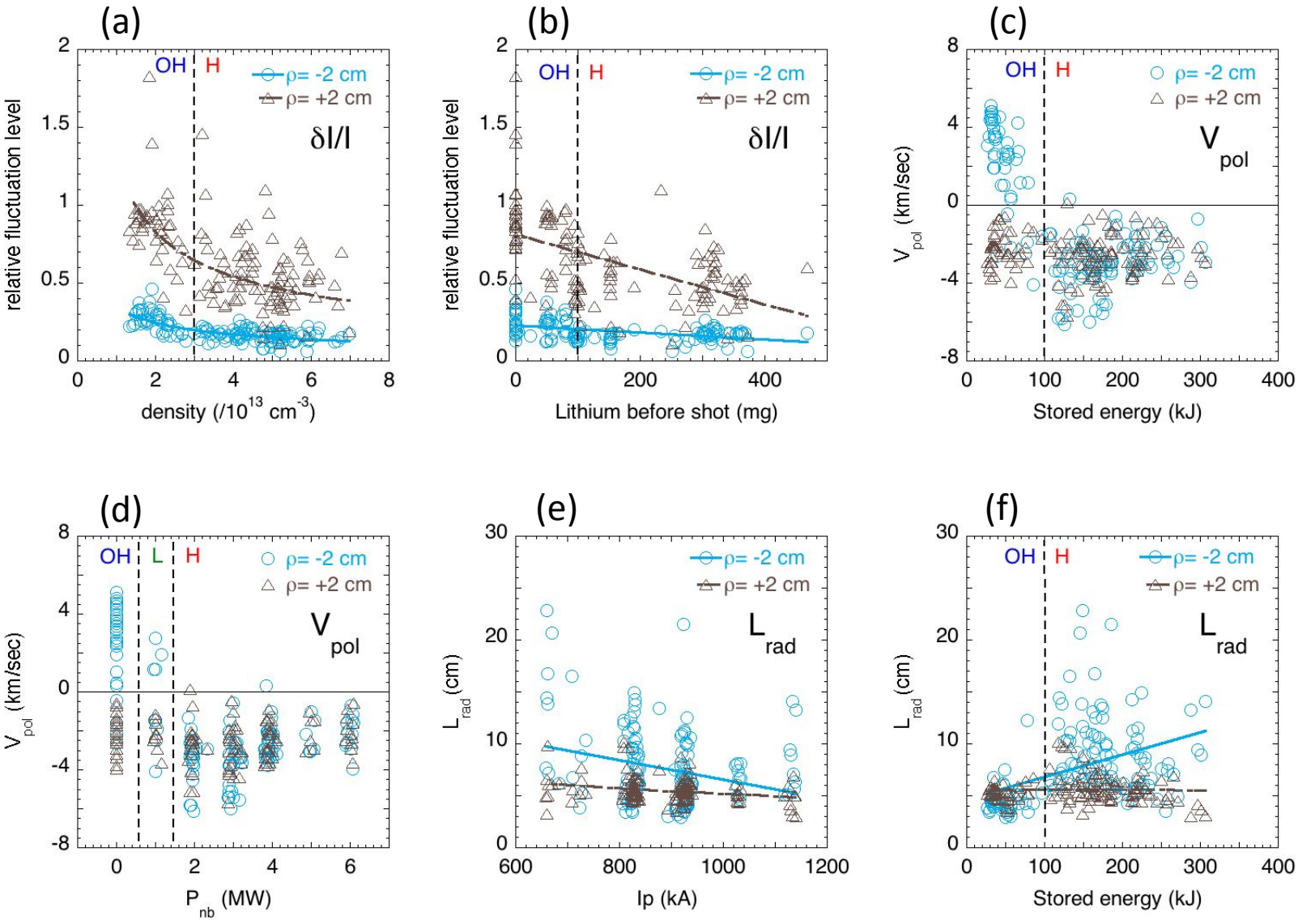
(a)
OH
H
ρ= -2 cm
ρ= +2 cm
δI/I
relative fluctuation level
density (/10^13 cm^-3)
(b)
OH
H
ρ= -2 cm
ρ= +2 cm
δI/I
relative fluctuation level
Lithium before shot (mg)
(c)
OH
H
ρ= -2 cm
ρ= +2 cm
V pol
V pol (km/sec)
Stored energy (kJ)
(d)
OH
L
H
ρ= -2 cm
ρ= +2 cm
V pol
V pol (km/sec)
P nb (MW)
(e)
ρ= -2 cm
ρ= +2 cm
L rad
L rad (cm)
Ip (kA)
(f)
OH
H
ρ= -2 cm
ρ= +2 cm
L rad
L rad (cm)
Stored energy (kJ)

Fig. 4

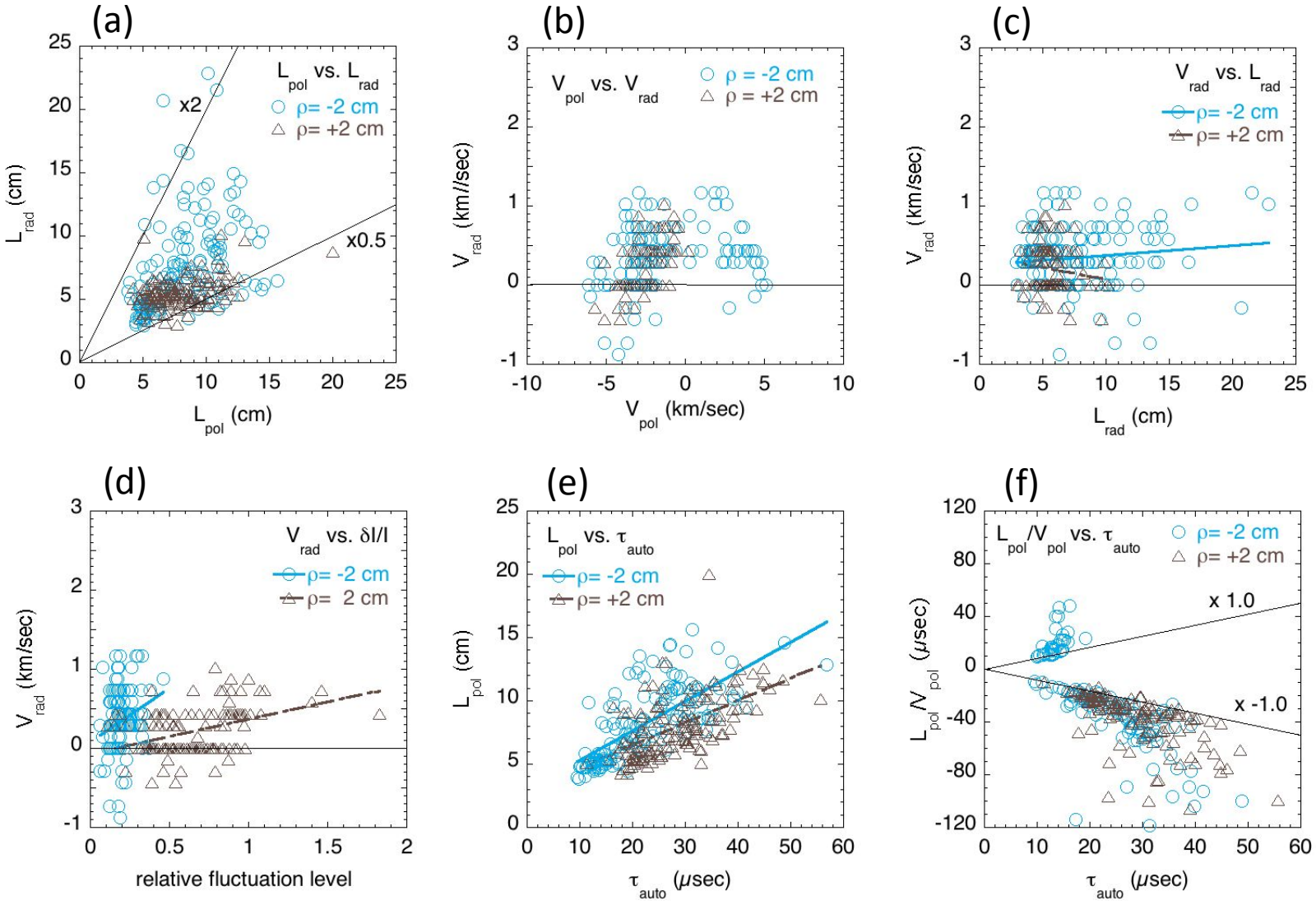
(a)
L_pol vs. L_rad
ρ= -2 cm
ρ= +2 cm
x2
x0.5
L_rad (cm)
L_pol (cm)
(b)
V_pol vs. V_rad
ρ = -2 cm
ρ = +2 cm
V_rad (km/sec)
V_pol (km/sec)
(c)
V_rad vs. L_rad
ρ= -2 cm
ρ= +2 cm
V_rad (km/sec)
L_rad (cm)
(d)
V_rad vs. δI/I
ρ= -2 cm
ρ= 2 cm
V_rad (km/sec)
relative fluctuation level
(e)
L_pol vs. τ_auto
ρ= -2 cm
ρ= +2 cm
L_pol (cm)
τ_auto (μsec)
(f)
L_pol/V_pol vs. τ_auto
ρ= -2 cm
ρ= +2 cm
x 1.0
x -1.0
L_pol/V_pol (μsec)
τ_auto (μsec)

Fig. 5

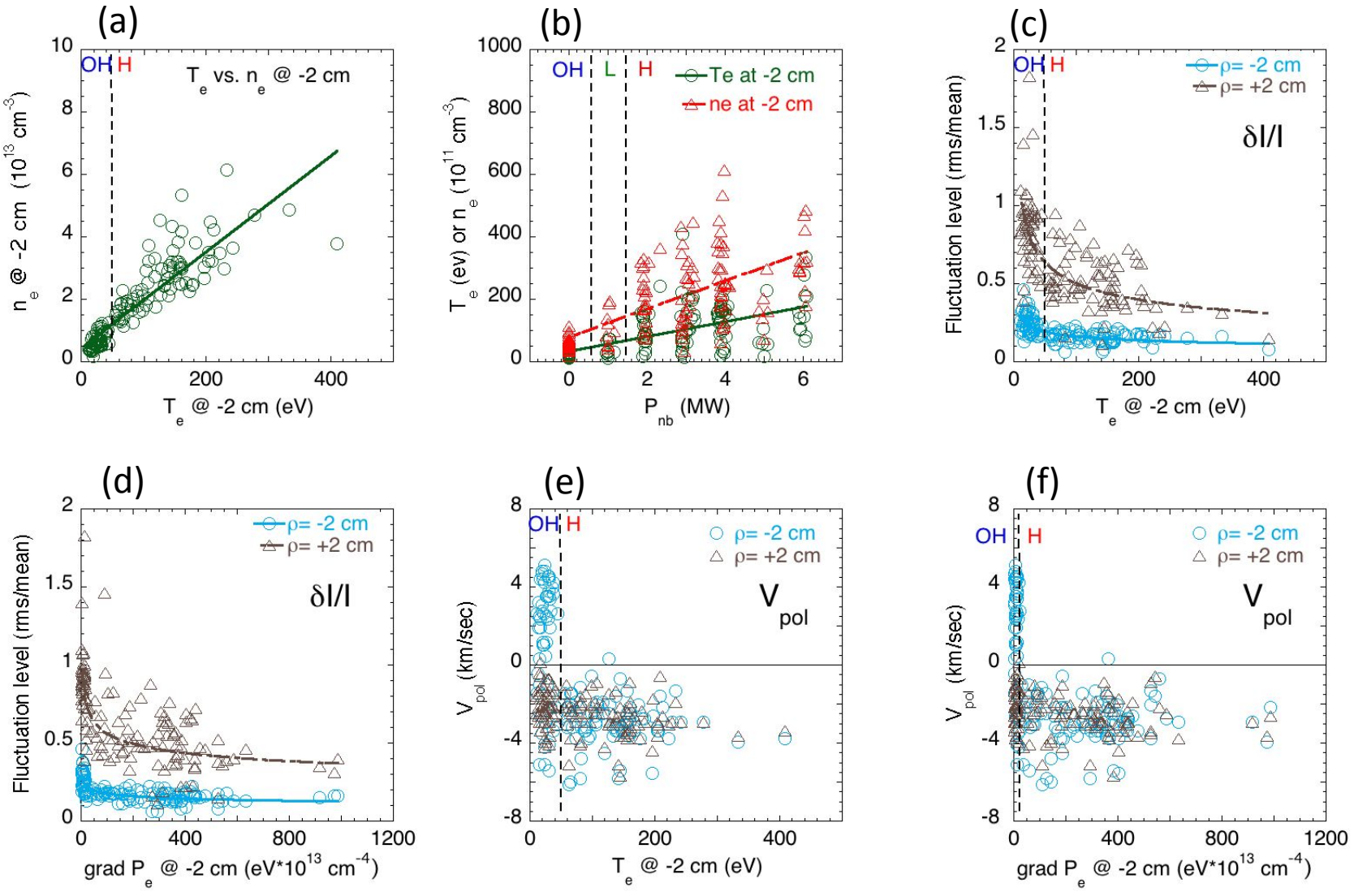
(a)
OH
H
T_e vs. n_e @ -2 cm
n_e @ -2 cm (10^13 cm^-3)
T_e @ -2 cm (eV)
(b)
OH
L
H
Te at -2 cm
ne at -2 cm
T_e (ev) or n_e (10^11 cm^-3)
P_nb (MW)
(c)
OH
H
ρ= -2 cm
ρ= +2 cm
δI/I
Fluctuation level (rms/mean)
T_e @ -2 cm (eV)
(d)
ρ= -2 cm
ρ= +2 cm
δI/I
Fluctuation level (rms/mean)
grad P_e @ -2 cm (eV*10^13 cm^-4)
(e)
OH
H
ρ= -2 cm
ρ= +2 cm
V_pol
V_pol (km/sec)
T_e @ -2 cm (eV)
(f)
OH
H
ρ= -2 cm
ρ= +2 cm
V_pol
V_pol (km/sec)
grad P_e @ -2 cm (eV*10^13 cm^-4)

Fig. 6

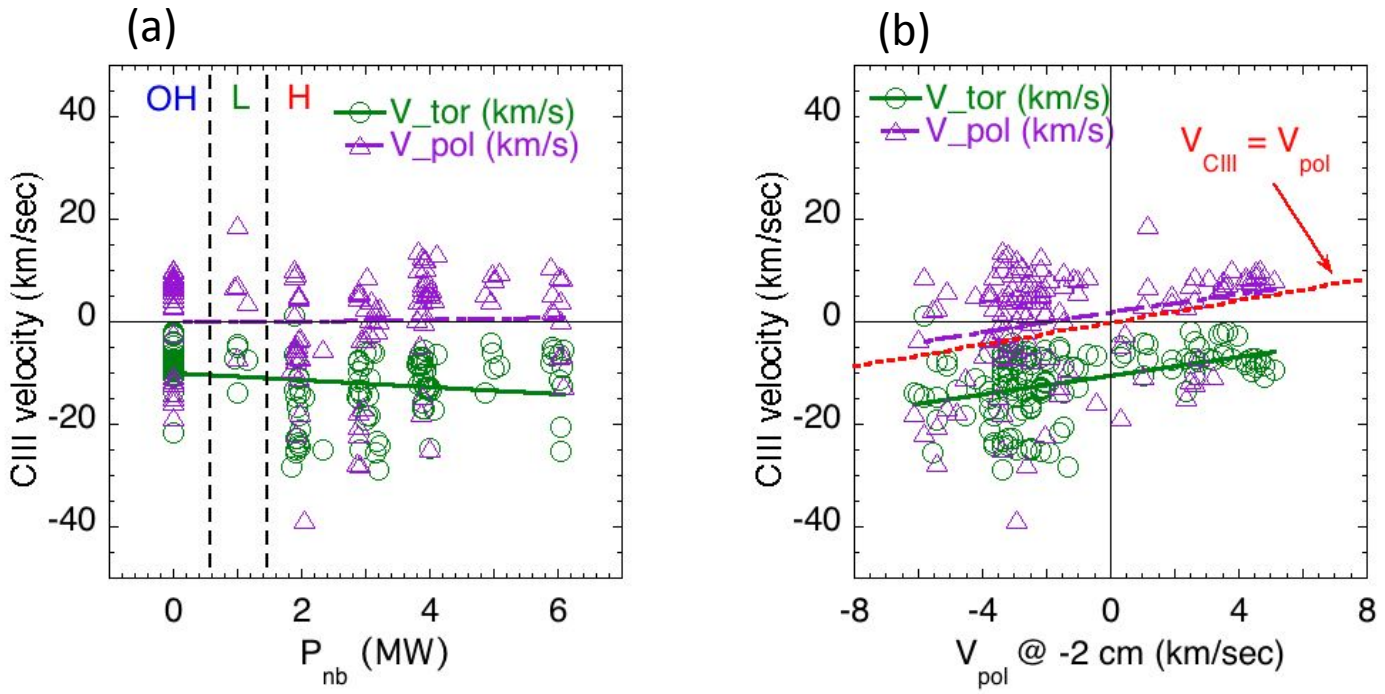
(a)
OH
L
H
V_tor (km/s)
V_pol (km/s)
CIII velocity (km/sec)
40
20
0
-20
-40
0
2
4
6
P nb (MW)
(b)
V_tor (km/s)
V_pol (km/s)
V CIII = V pol
CIII velocity (km/sec)
-8
-4
0
4
8
V pol @ -2 cm (km/sec)

Fig. 7

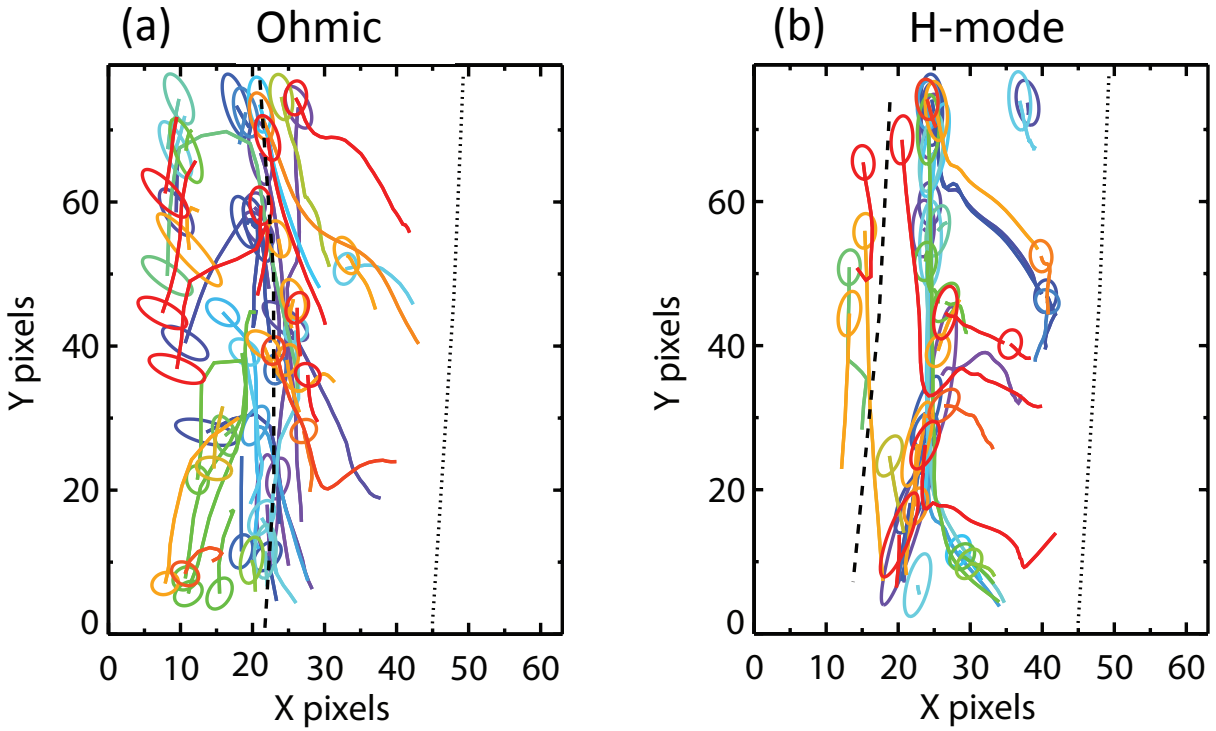

Fig. 8

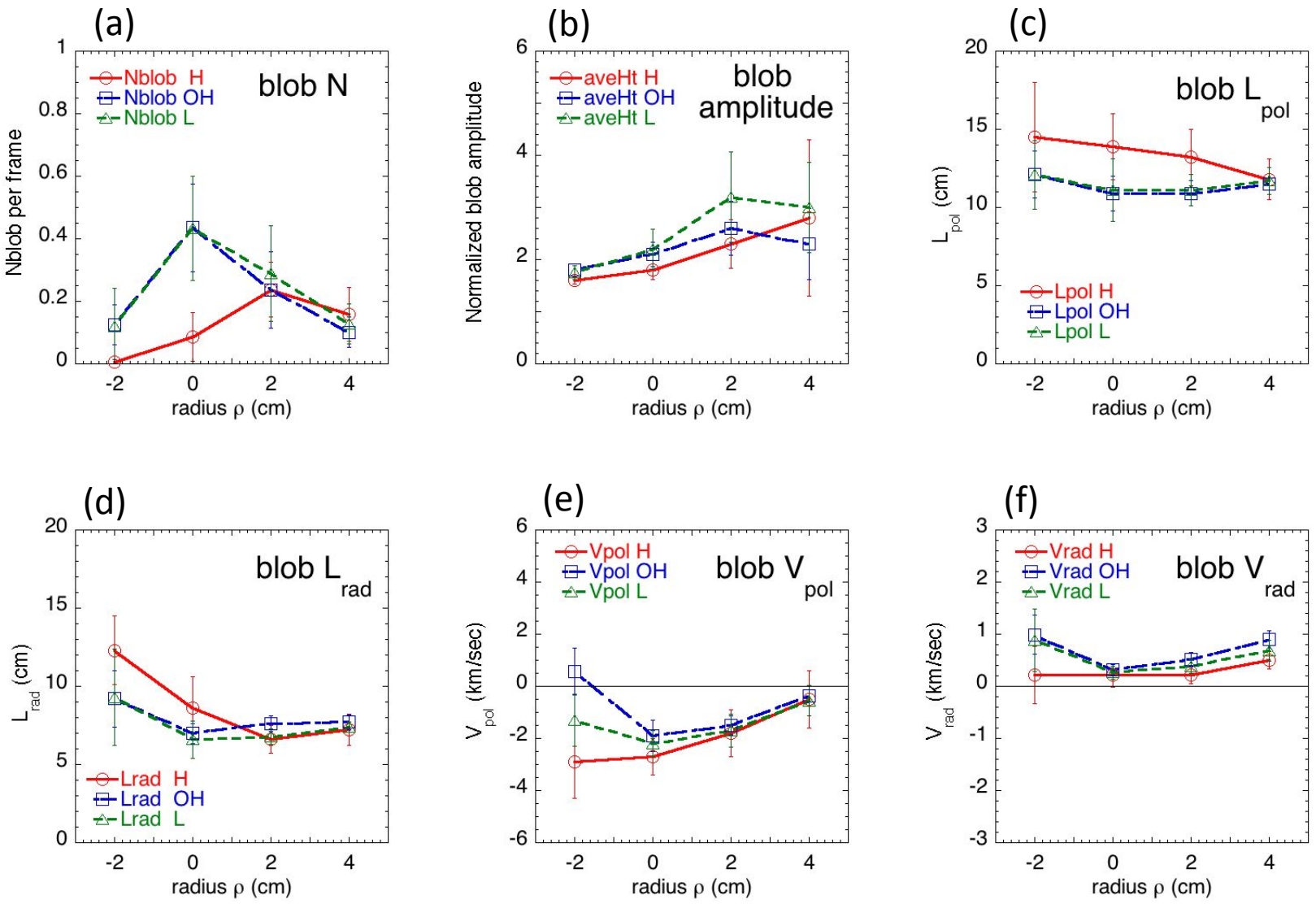
(a)
blob N
Nblob H
Nblob OH
Nblob L
Nblob per frame
radius ρ (cm)
(b)
blob amplitude
aveHt H
aveHt OH
aveHt L
Normalized blob amplitude
radius ρ (cm)
(c)
blob L pol
Lpol H
Lpol OH
Lpol L
L pol (cm)
radius ρ (cm)
(d)
blob L rad
Lrad H
Lrad OH
Lrad L
L rad (cm)
radius ρ (cm)
(e)
blob V pol
Vpol H
Vpol OH
Vpol L
V pol (km/sec)
radius ρ (cm)
(f)
blob V rad
Vrad H
Vrad OH
Vrad L
V rad (km/sec)
radius ρ (cm)

Fig. 9

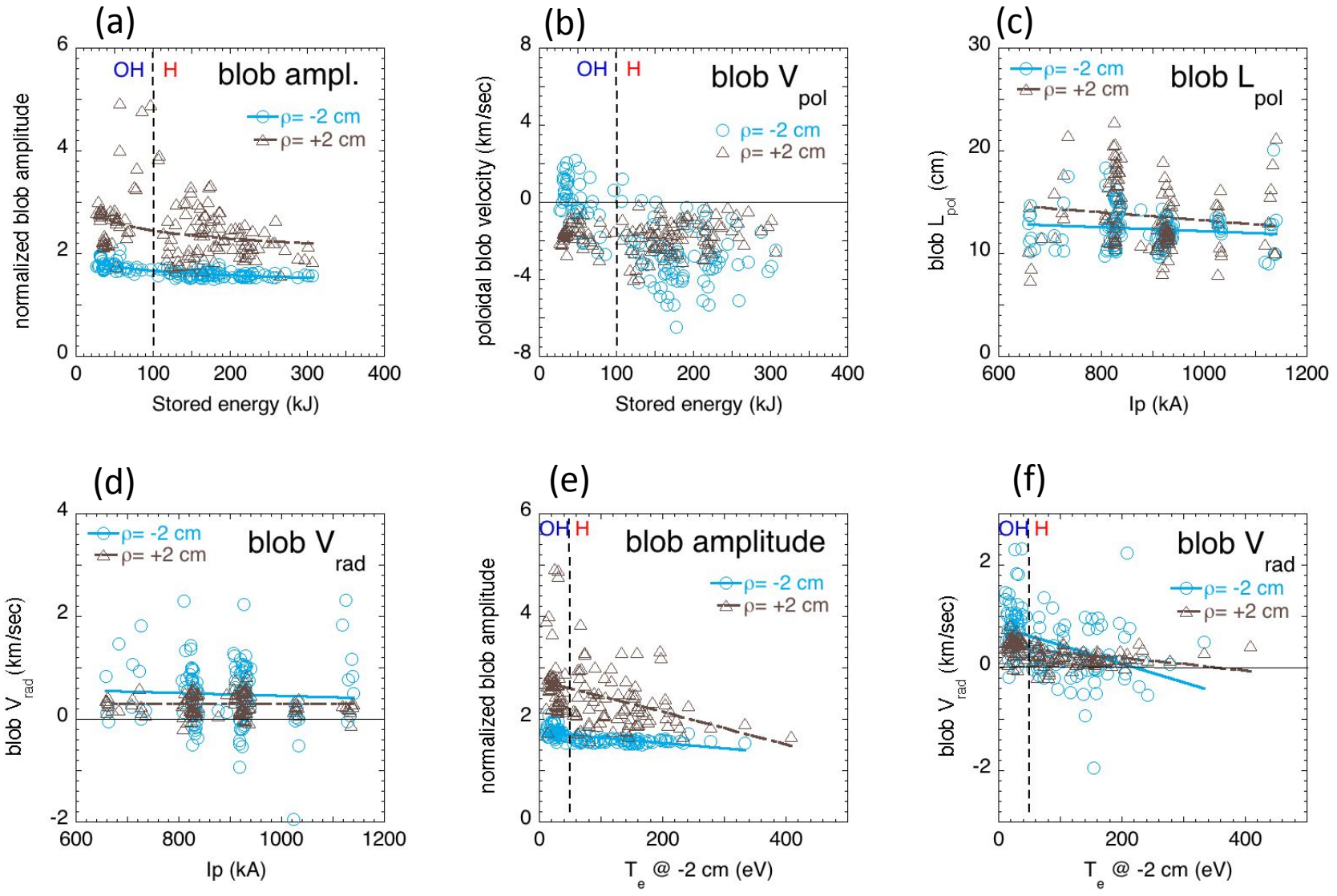
(a)
OH
H
blob ampl.
ρ= -2 cm
ρ= +2 cm
normalized blob amplitude
Stored energy (kJ)
(b)
blob V pol
poloidal blob velocity (km/sec)
(c)
blob L pol
blob L pol (cm)
Ip (kA)
(d)
blob V rad
blob V rad (km/sec)
(e)
blob amplitude
T e @ -2 cm (eV)
(f)

Fig. 10

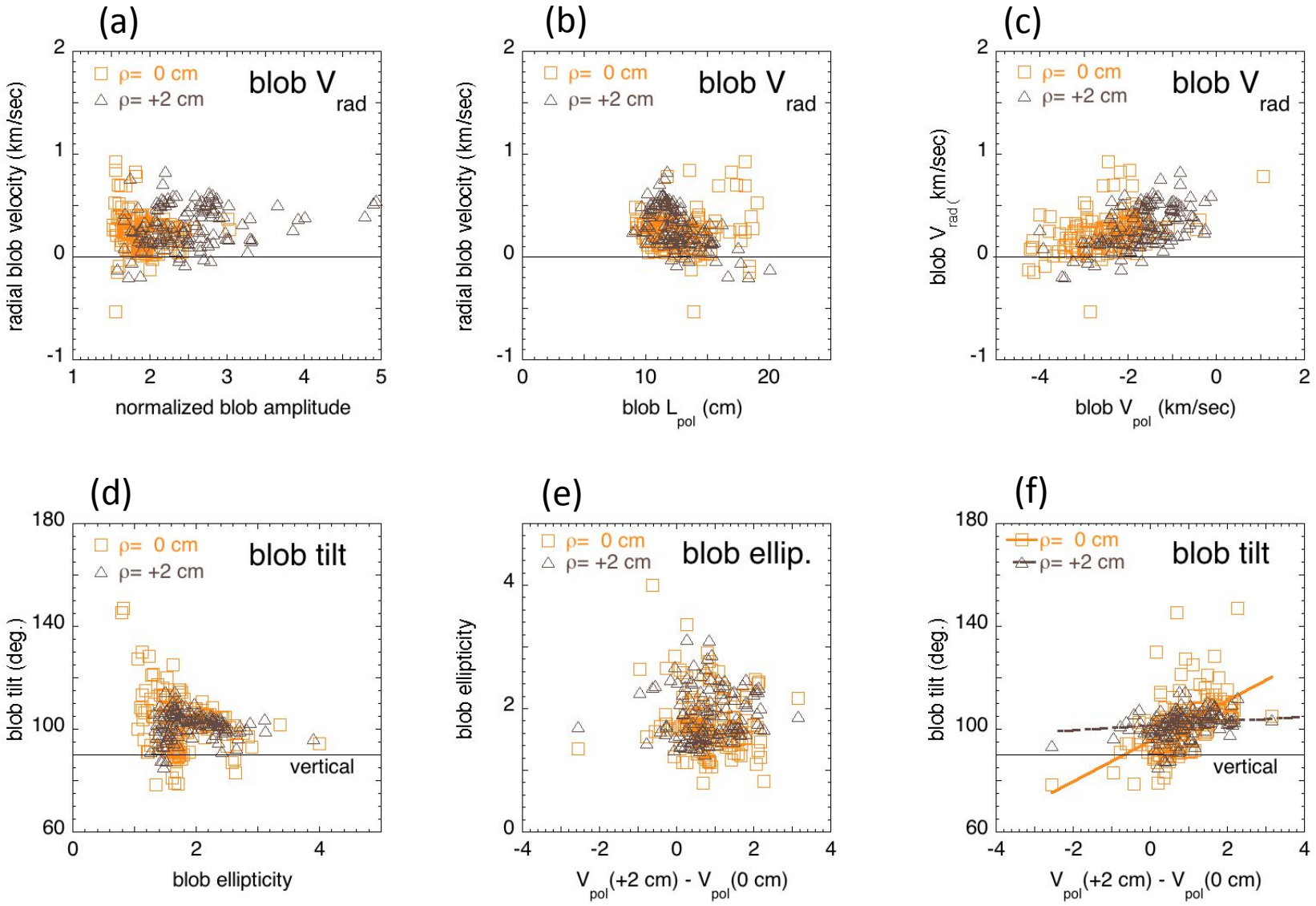
(a)
ρ= 0 cm
ρ= +2 cm
blob V rad
radial blob velocity (km/sec)
normalized blob amplitude
(b)
ρ= 0 cm
ρ= +2 cm
blob V rad
radial blob velocity (km/sec)
blob L pol (cm)
(c)
ρ= 0 cm
ρ= +2 cm
blob V rad
blob V rad (km/sec)
blob V pol (km/sec)
(d)
ρ= 0 cm
ρ= +2 cm
blob tilt
blob tilt (deg.)
vertical
blob ellipticity
(e)
ρ= 0 cm
ρ= +2 cm
blob ellip.
blob ellipticity
V pol(+2 cm) - V pol(0 cm)
(f)
ρ= 0 cm
ρ= +2 cm
blob tilt
blob tilt (deg.)
vertical
V pol(+2 cm) - V pol(0 cm)

Fig. 11

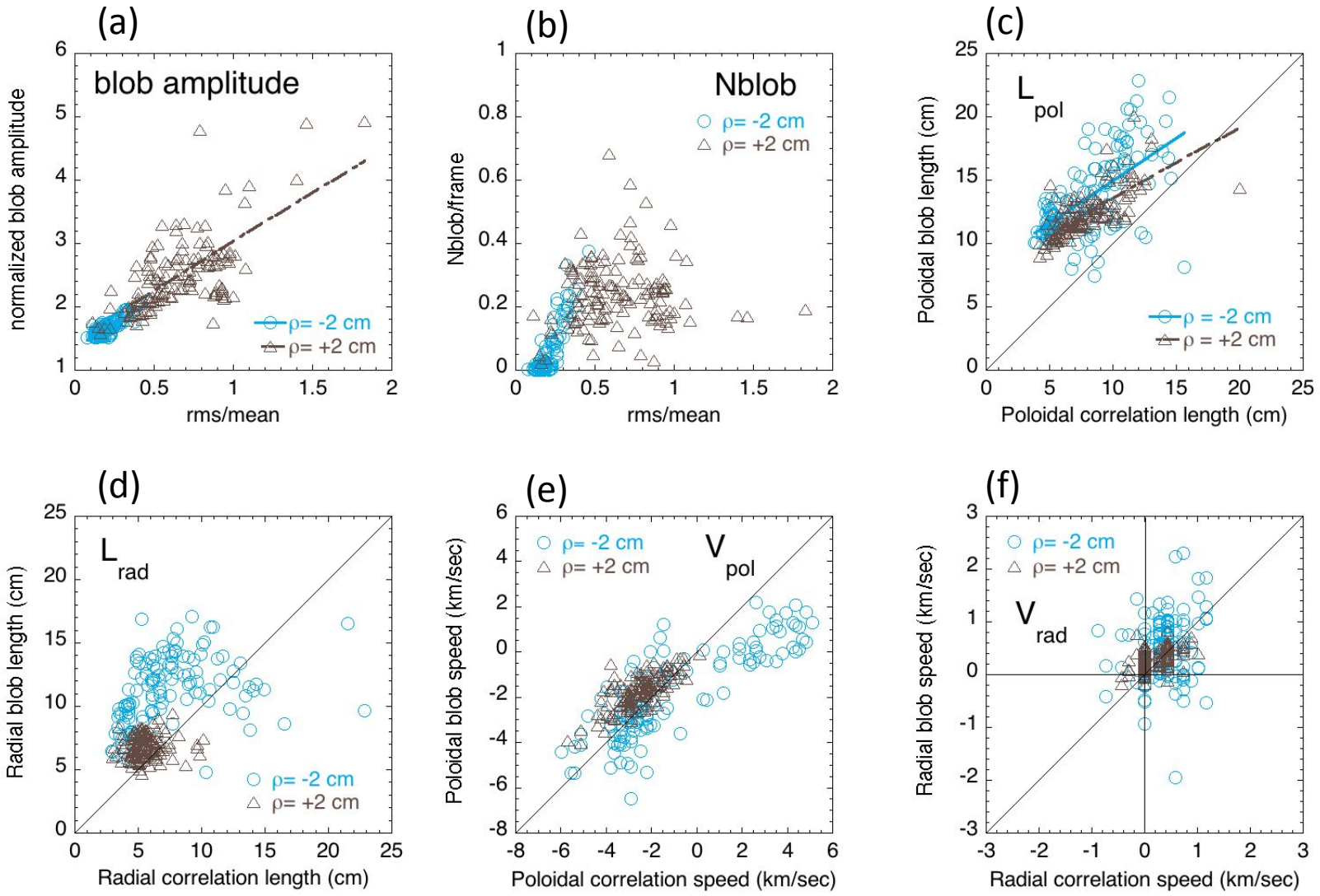
(a)
blob amplitude
normalized blob amplitude
rms/mean
ρ= -2 cm
ρ= +2 cm
(b)
Nblob
Nblob/frame
rms/mean
ρ= -2 cm
ρ= +2 cm
(c)
L pol
Poloidal blob length (cm)
Poloidal correlation length (cm)
ρ = -2 cm
ρ = +2 cm
(d)
L rad
Radial blob length (cm)
Radial correlation length (cm)
ρ= -2 cm
ρ= +2 cm
(e)
V pol
Poloidal blob speed (km/sec)
Poloidal correlation speed (km/sec)
ρ= -2 cm
ρ= +2 cm
(f)
V rad
Radial blob speed (km/sec)
Radial correlation speed (km/sec)
ρ= -2 cm
ρ= +2 cm

Fig. 12

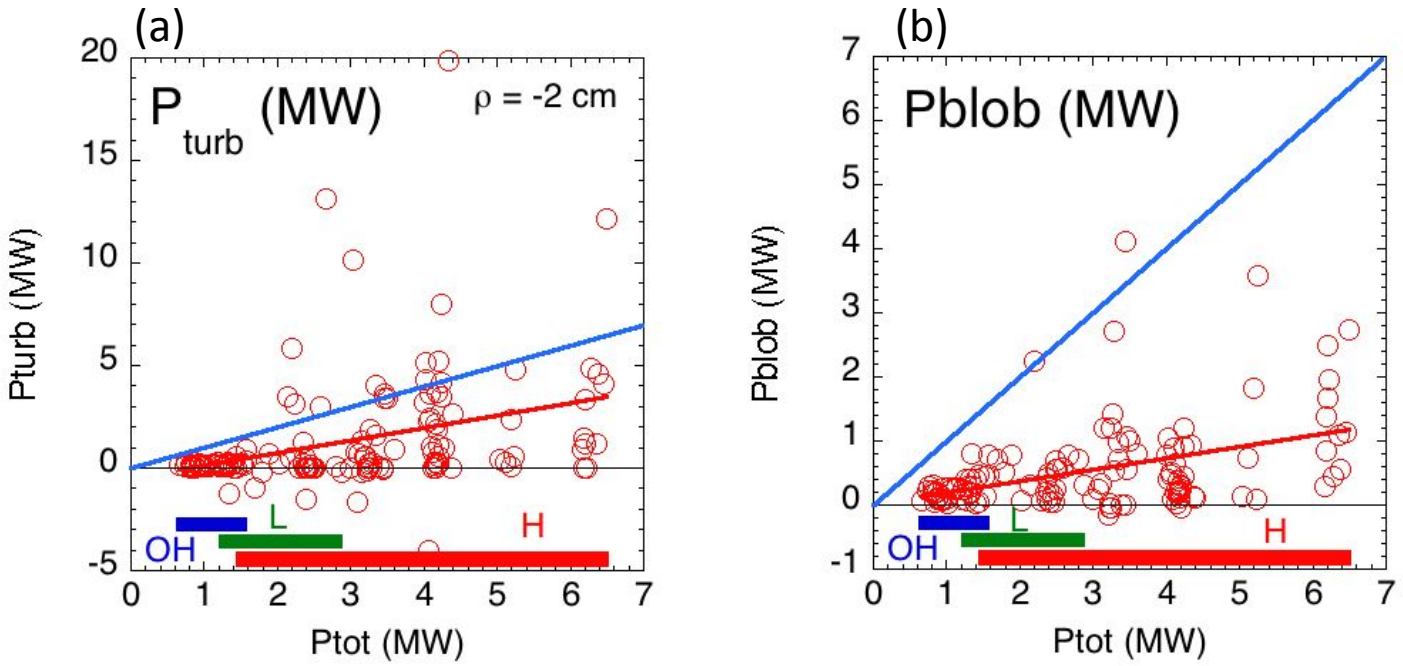
(a)
P turb (MW)
ρ = -2 cm
Pturb (MW)
Ptot (MW)
OH
L
H
(b)
Pblob (MW)
Pblob (MW)
Ptot (MW)
OH
L
H

Fig. 13

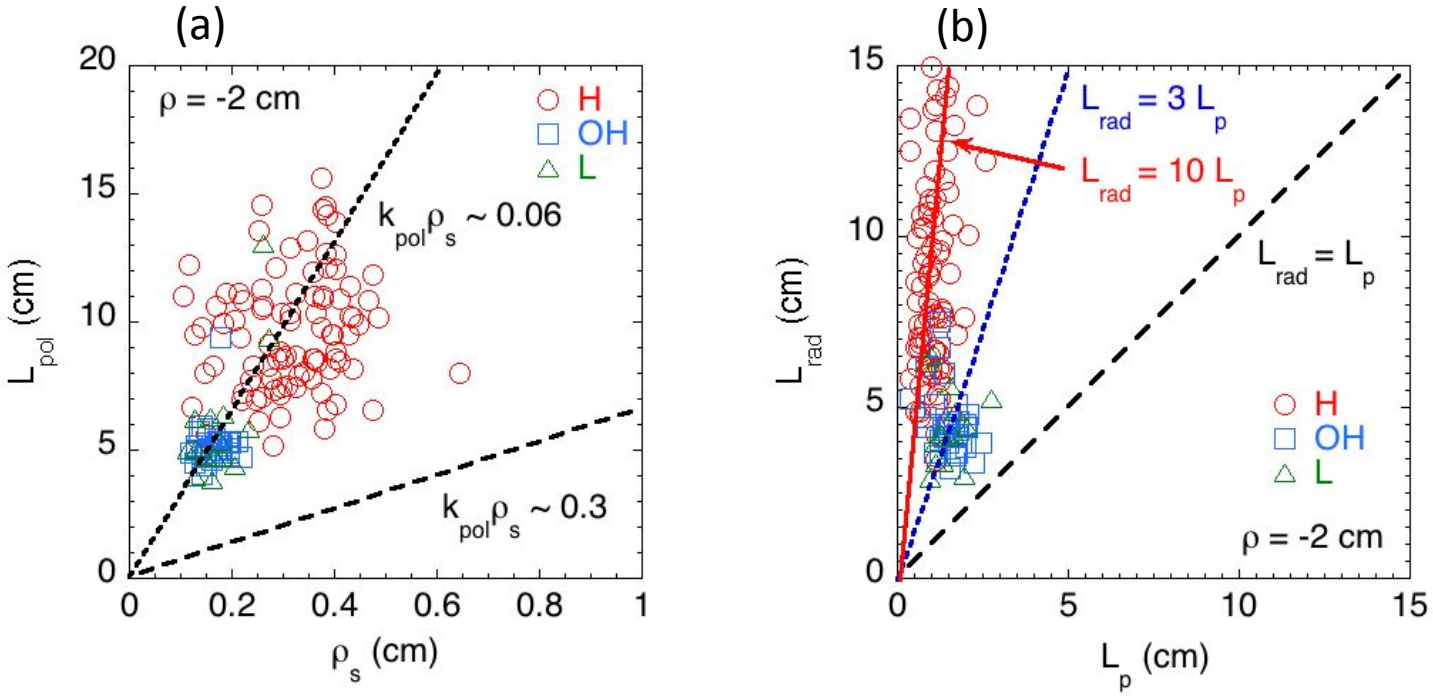
(a)
ρ = -2 cm
H
OH
L
k_pol ρ_s ~ 0.06
k_pol ρ_s ~ 0.3
L_pol (cm)
ρ_s (cm)
0
5
10
15
20
0.2
0.4
0.6
0.8
1
(b)
L_rad = 3 L_p
L_rad = 10 L_p
L_rad = L_p
H
OH
L
ρ = -2 cm
L_rad (cm)
L_p (cm)

Fig. 14

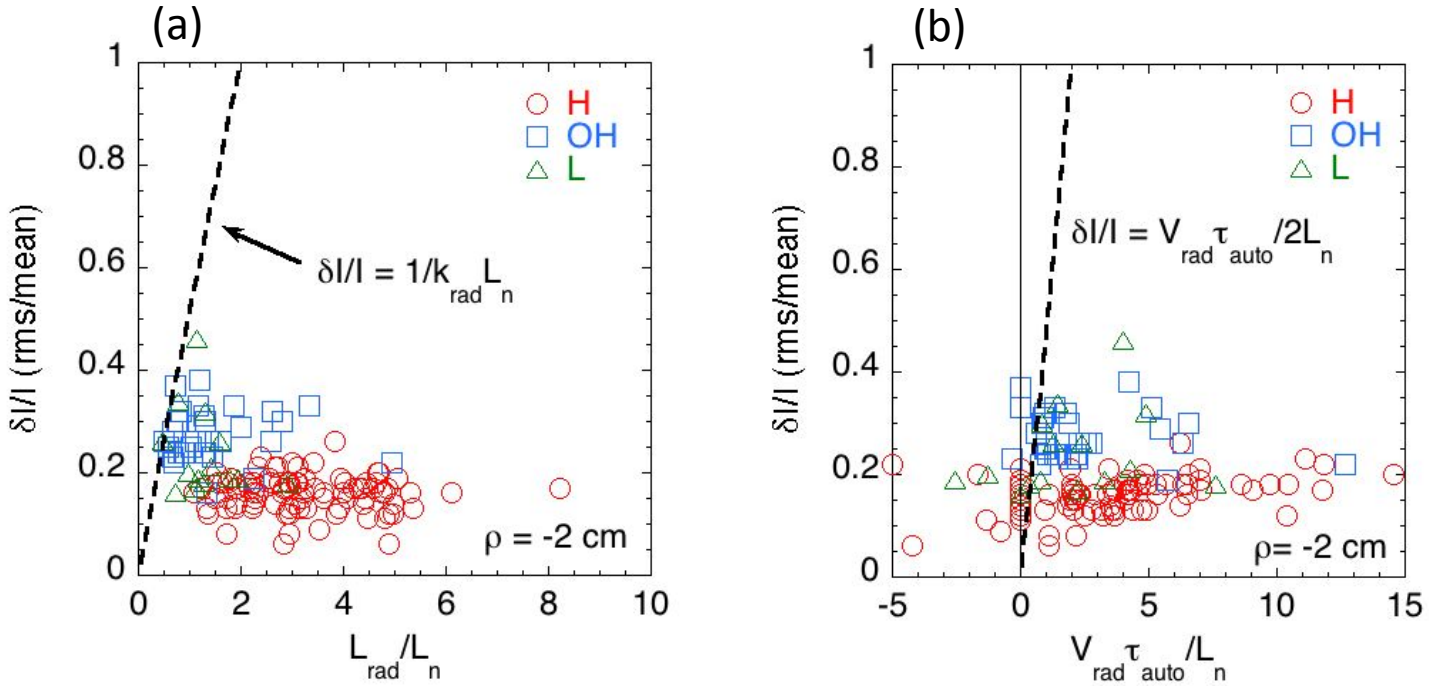
(a)
δI/I (rms/mean)
1
0.8
0.6
0.4
0.2
0
0
2
4
6
8
10
L_rad/L_n
H
OH
L
δI/I = 1/k_rad L_n
ρ = -2 cm
(b)
δI/I (rms/mean)
1
0.8
0.6
0.4
0.2
0
-5
0
5
10
15
V_rad τ_auto/L_n
H
OH
L
δI/I = V_rad τ_auto/2L_n
ρ= -2 cm

Fig. 15

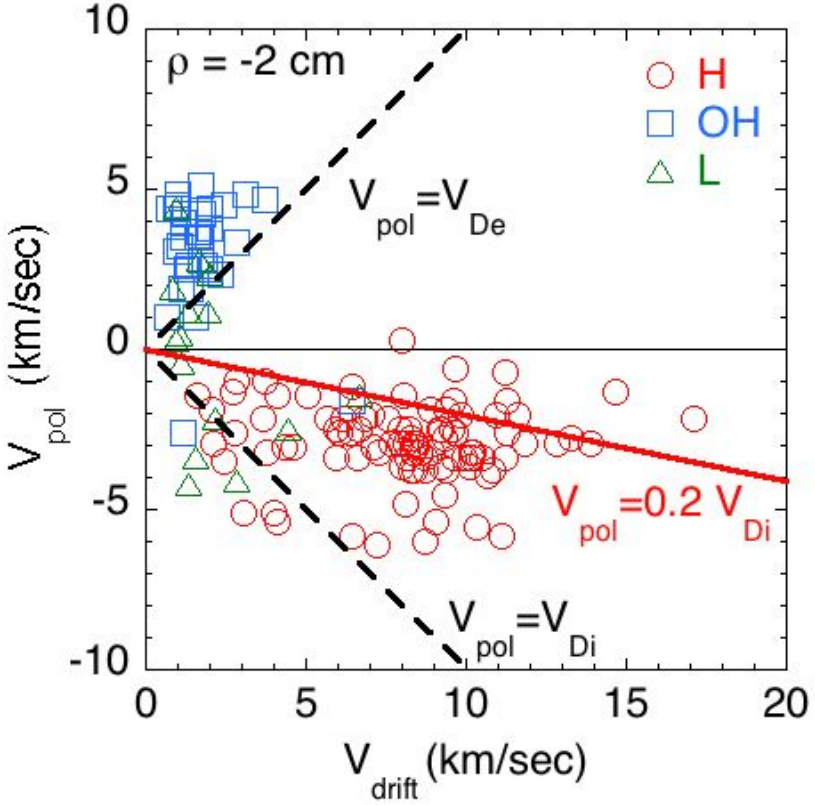
ρ = -2 cm
H
OH
L
V_pol=V_De
V_pol=0.2 V_Di
V_pol=V_Di
V_pol (km/sec)
V_drift (km/sec)
10
5
0
-5
-10
0
5
10
15
20

Fig. 16

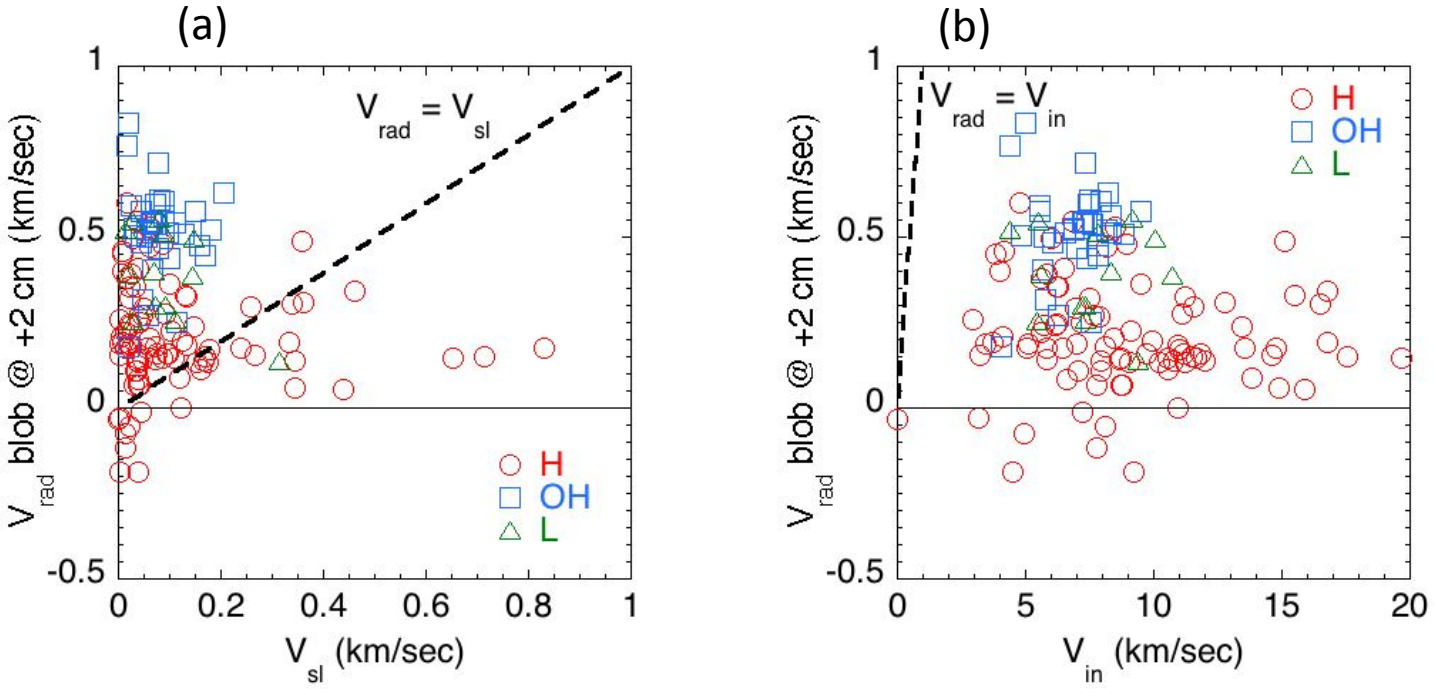
(a)
(b)
V rad = V sl
V rad = V in
H
OH
L
V rad blob @ +2 cm (km/sec)
V sl (km/sec)
V in (km/sec)
1
0.5
0
-0.5
0
0.2
0.4
0.6
0.8
1
5
10
15
20

Fig. 17

Princeton Plasma Physics Laboratory
Office of Reports and Publications

Managed by
Princeton University

under contract with the
U.S. Department of Energy
(DE-AC02-09CH11466)

P.O. Box 451, Princeton, NJ 08543
Phone: 609-243-2245
Fax: 609-243-2751

E-mail: publications@pppl.gov
Website: http://www.pppl.gov